

A Multi-wavelength Survey of AGN in Massive Clusters: AGN Detection and Cluster AGN Fraction

Alison J. Klesman^{1*} and Vicki L. Sarajedini¹

¹ *University of Florida, Department of Astronomy, 211 Bryant Space Science Center, FL, 32611 USA*

2 August 2012

ABSTRACT

We aim to study the effect of environment on the presence and fuelling of Active Galactic Nuclei (AGN) in massive galaxy clusters. We explore the use of different AGN detection techniques with the goal of selecting AGN across a broad range of luminosities, AGN/host galaxy flux ratios, and obscuration levels. From a sample of 12 galaxy clusters at redshifts $0.5 < z < 0.9$, we identify AGN candidates using optical variability from multi-epoch HST imaging, X-ray point sources in Chandra images, and mid-IR SED power-law fits through the Spitzer IRAC channels. We find 178 optical variables, 74 X-ray point sources, and 64 IR power law sources, resulting in an average of ~ 25 AGN per cluster. We find no significant difference between the fraction of AGN among galaxies in clusters and the percentage of similarly-detected AGN in field galaxy studies ($\sim 2.5\%$). This result provides evidence that galaxies are still able to fuel accretion onto their supermassive black holes, even in dense environments. We also investigate correlations between the percentage of AGN and cluster physical properties such as mass, X-ray luminosity, size, morphology class and redshift. We find no significant correlations among cluster properties and the percentage of AGN detected.

Key words: galaxies: active, galaxies: clusters: general, galaxies: evolution, galaxies: statistics, infrared: galaxies, X-rays: galaxies: clusters

* E-mail: alichan@astro.ufl.edu (AJK); vicki@astro.ufl.edu (VLS)

1 INTRODUCTION

Active Galactic Nuclei (AGN) are envisioned to be accreting supermassive black holes at the centres of galaxies, with masses ranging from $\sim 10^6$ – $10^{10} M_{\odot}$ (e.g., Salpeter 1964; Lynden-Bell 1969). Supermassive black holes are now believed to reside in the centre of all massive galaxies (Kormendy & Richstone 1995), and there is a well-established correlation between the mass of the central black hole and the mass and velocity dispersion of the host galaxy's spheroidal component (Magorrian et al. 1998; Ferrarese & Merritt 2000; Gebhardt et al. 2000). This relationship indicates that there is a fundamental link between the growth of supermassive black holes and the formation of the galaxies in which they reside. The first challenge to understanding this link, is the unbiased identification of AGN in galaxy surveys. While AGN are identified using a range of techniques (emission line characteristics, optical and IR colour selection, X-ray emission, radio emission, and variability), many produce an incomplete picture of AGN, as they can be biased against galaxies in which the AGN light is not a significant percentage of the total galaxy light. Optical and UV surveys can also miss more heavily obscured AGN and host galaxies. Therefore, it is necessary to utilise more than one technique to select a more complete sample of AGN to study the links between these objects and the galaxies in which they reside.

AGN show variability on a variety of timescales. The optical line emission and continuum flux from quasars has been observed to vary on timescales of months to years, while X-ray flux from these sources varies on shorter timescales of hours to days (Peterson 2001 & references therein). It has been shown that 80–100% of AGN candidates display variability up to several percent in the optical over the course of several years (e.g., Koo et al. 1986; McLeod & Bechtold 2010). The use of small aperture photometry with high-resolution HST images allows for the detection of varying AGN comprising as little as $\sim 5\%$ of the total optical galaxy light (Sarajedini et al. 2000, 2003, 2006). Klesman & Sarajedini (2007) investigate the use of multi-wavelength AGN identification techniques by conducting a variability study on a pre-selected sample of X-ray and mid-IR AGN in the Great Observatories Origins Deep Survey (GOODS) South field. They found that 26% of all AGN candidates (either X-ray or mid-IR selected) are optically varying on timescales of several months. The fraction of optical variables increases to 51% when considering sources displaying softer X-ray spectra. While unobscured AGN appear to have the most significant optical variability, some obscured AGN were also observed as optical variables. The overall survey results revealed

that 2% of all galaxies in the GOODS North and South fields appear to host varying AGN (Sarajedini et al. 2011).

AGN are also known to be luminous X-ray sources and can be routinely selected from deep X-ray (<10 keV) surveys. The X-ray emission is believed to originate very close to the central black hole and is produced by Compton upscattering of softer photons by a hot “corona” around the accretion disk (e.g., Sunyaev & Titarchuk 1980). X-ray, UV, and optical emission can be absorbed by dust surrounding the nucleus, and then reprocessed and re-radiated as infrared light. Donley et al. (2008) find that a power-law fit to photometric measurements through the mid-IR bands can also be used to identify AGN and does so more reliably than using IR colours alone (e.g. Lacy et al. 2004).

Galaxy clusters present a unique environment in which to explore the link between AGN and their host galaxies. The dense cluster environment is known to impact galaxy morphology since a larger fraction of early-type galaxies are found among clusters than that found among field galaxies (e.g., Hubble & Humason 1931; Morgan 1961; Abell 1965; Oemler 1974). However, galaxies in clusters encounter each other at higher relative speeds, resulting in fewer mergers among cluster galaxies than in more loosely bound groups (e.g., Makino & Hut 1997). Early spectroscopic studies (Gisler 1978; Dressler et al. 1985) presented evidence that AGN may be less common in rich clusters than in the field. These studies concluded that the fraction of AGN in clusters is about 1%, compared with 5% observed in the field (Dressler et al. 1985). This view has been challenged by recent X-ray surveys which have detected large numbers of optically normal cluster galaxies whose luminous X-ray emission would indicate AGN activity (e.g., Martini et al. 2002, 2006). Using X-ray observations, Martini et al. (2002) found a cluster AGN fraction approximately 5 times higher than that found by Dressler et al. (1985). To fully address the AGN fraction in clusters and understand the role environment plays requires cluster surveys that identify AGN having a broad range of luminosities and obscuration levels.

In this paper, we will explore the issue of AGN identification in cluster galaxies using a multi-wavelength, multi-technique approach to produce a largely unbiased sample with which to investigate the relationship between AGN, their environment, and their host galaxies. We present our sample of 12 massive galaxy clusters at $z = 0.5\text{--}0.9$ in Section 2. In Sections 3, 4, and 5, we apply the techniques of optical variability, X-ray emission, and IR power-law SED fitting to identify AGN in these clusters. In Section 6, we compare the various identification techniques to explore completeness issues. We determine cluster membership probabilities

for the galaxies in our images and calculate the percentage of AGN in clusters in Sections 7 and 8. Finally, we present our conclusions in Section 9. Throughout the paper we assume a standard cosmology with $H_0 = 70$, $\Omega_M = 0.3$, and $\Omega_\Lambda = 0.7$.

2 GALAXY CLUSTER SAMPLE

To investigate the role of environment on the AGN phenomenon, we selected several galaxy clusters to perform a census of AGN. We chose clusters for which archival data was available that would allow AGN to be detected via optical variability, X-ray emission, and mid-Infrared properties. All of the galaxy clusters used in this work are part of a sample observed multiple times with the Hubble Space Telescope (HST) Advanced Camera for Surveys (ACS) in a survey for supernovae in massive high-redshift clusters (HST programs GO 10493, cycle 14 and GO 10793, cycle 15, P.I. Avishay Gal-Yam). Our sample consists of 12 clusters with redshifts ranging from 0.50–0.89. All have also been observed with the Chandra X-ray observatory, and seven have been imaged in the mid-IR with the Spitzer IRAC instrument. Table 1 lists the clusters, their redshifts, and the number of optical ACS epochs from the survey (Sharon et al. 2010, Table 1). The table also lists whether Spitzer data are available for the clusters.

2.1 MACS Clusters

Seven of the clusters in this work are part of the Massive Cluster Survey (MACS) (Ebeling et al. 2001). This survey targets distant ($z > 0.3$), luminous ($L_X > 10^{44}$ erg/s), and therefore massive galaxy clusters selected from the ROSAT All-Sky Survey. Detailed optical and X-ray observations were carried out by Barrett (2006), including spectroscopic confirmation of cluster members, mass, velocity dispersion, and virial radius determinations. Stott et al. (2007) report the X-ray luminosities for these clusters. These values are also listed in Table 2.

We note that the virial masses of the MACS clusters found in Table 2 are actually measures of $M_{X,200}$ derived by Barrett (2006) from the X-ray emitting gas mass within the virial radius r_v assuming the gas is a perfect gas in hydrostatic equilibrium, isothermal, and spherically symmetric. This mass was used as a proxy for the virial mass determined using the position and velocity dispersion of cluster galaxies, as measurements of M_{200} using this method require a large number of galaxy redshifts, which is difficult and time-consuming, especially for more distant clusters. Barrett (2006) examines the correlation between clus-

ter virial mass measured via these two methods, using an average of ~ 40 galaxy redshifts per cluster, and finds the two agree to within 15%. This difference appears to arise from poor sampling of galaxies when determining the virial mass, and is similar to the findings of Reiprich & Böhringer (2002), who find an agreement of $\sim 25\%$ between virial masses determined via X-ray gas and galaxy dynamics with a similar sampling of ~ 40 galaxies per cluster. Rines et al. (2003) find that the virial mass determination given by these two methods agrees well when using a sample of ~ 200 galaxies to determine the virial mass via galaxy dynamics.

2.2 CL0152-1357

CL0152 has a bolometric X-ray luminosity of $L_X = 1.6 \times 10^{45}$ erg/s (Maughan et al. 2003) and a virial radius r_{200} of 1.14 Mpc (Jee et al. 2005a). The cluster shows significant substructure in its X-ray morphology indicative of an ongoing merger, with two peaks in its X-ray morphology that correspond to two subclusters first identified by Ebeling et al. (2000) and later confirmed by Maughan et al. (2003). Both subclusters show similar temperatures of ~ 5.6 keV (Maughan et al. 2003). A catalog of 102 confirmed cluster members has been published by Demarco et al. (2005).

2.3 CLJ1226.9+3332

CLJ1226 has a bolometric X-ray luminosity of $L_X = 5.3 \times 10^{45}$ erg/s, an X-ray temperature of $T_X = 11.5$ keV, and a total mass $M = 1.4 \times 10^{15} M_\odot$ with a virial radius of 1.66 Mpc (Maughan et al. 2004). Ellis et al. (2006) identified 45 spectroscopically-confirmed cluster members. CLJ1226 shows little dynamic activity and relaxed X-ray emission, although XMM and Chandra observations have revealed an asymmetry in the temperature distribution indicative of a merger event in the cluster (Maughan et al. 2007).

2.4 MS0451.6-0305

MS0451 has a bolometric X-ray luminosity of $L_X = 2.01 \times 10^{45}$ erg/s and an X-ray temperature of $T_X = 10.0$ keV (Donahue et al. 2003). The cluster has an elongated but smooth distribution of galaxies, and Moran et al. (2007) identified 319 spectroscopically-confirmed cluster members between $0.52 < z < 0.56$. It has a virial radius of 2.6 Mpc (Moran et al. 2007) and a M_{200} of $1.4 \times 10^{15} M_\odot$ (Donahue et al. 2003). Moran et al. (2007) speculate that

physical processes related to the intracluster medium (ICM) which are important in the evolution of currently infalling galaxies, such as gas starvation and ram pressure stripping, begin to affect galaxies at a large radius (e.g., $r \sim 3.5\text{--}5.5$ Mpc for merging, $0\text{--}2.5$ Mpc for ram pressure stripping, $0\text{--}3.5$ Mpc for starvation, and $0\text{--}5$ Mpc for harassment). Molnar et al. (2002) identified 14 unresolved X-ray point sources in the field of MS0451, though they claim this number is within 1σ of the number expected from a non-cluster background field.

2.5 MS1054.4-0321

MS1054 is an Abell class 3 cluster with a bolometric X-ray luminosity $L_X = 23.3 \times 10^{44}$ erg/s (Stott et al. 2007) and a virial mass $M_{200} = 1.1 \times 10^{15} M_\odot$ (Jee et al. 2005b). Substructure in the distribution of galaxies matches diffuse soft X-ray emission, and weak lensing indicates that the cluster is young, massive, and still relaxing (Hoekstra et al. 2000). Tran et al. (1999) found a virial radius for the cluster of 1.8 Mpc. In addition to ACS and ground-based optical and IR imaging, there have been spectroscopic surveys of this cluster using Keck (e.g., van Dokkum et al. 2000; Tran et al. 2007) to determine cluster membership of many galaxies in the ACS images.

2.6 SDSS1004+41

SDSS1004 contains the quadruply-lensed background quasar SDSS J1004+4112 at $z = 1.734$ (Inada et al. 2003); there is also a faint fifth image projected through the cluster Brightest Cluster Galaxy (BCG) (Inada et al. 2005). Williams & Saha (2004) modelled the cluster and calculated a virial radius of $1\text{--}1.5$ Mpc and a virial mass $M_{200} = 4.2 \times 10^{14} M_\odot$. Oguri (2010) determine that the core of SDSS1004 is highly evolved and a comparison between SDSS1004 and MACSJ1423 by Limousin et al. (2010) shows that the two clusters are very similar based on the distribution of their mass, light, and gas. We adopt a virial radius of 1.35 Mpc for SDSS1004 for this study, as it is the value of the virial radius of MACSJ1423 and falls in the middle of the range suggested by Williams & Saha (2004).

3 OPTICAL VARIABILITY

Each cluster in our sample has 2–3 epochs of ACS observations in the *I*-band (either F775W or F814W). Exposure times range from $\sim 4000\text{--}9000$ s and epochs are typically spaced one year apart (see Table 3). The high resolution of HST allows the nuclei of galaxies to be

accurately targeted for small aperture photometry ($r_{\text{aperture}} = 0''.09$), which allows us to minimise the contribution of light from the host galaxy when searching for nuclear variability from lower luminosity AGN which might otherwise be masked by their hosts. Eleven of the twelve clusters were also observed for one epoch in a second optical filter (F625W, F606W, or F555W). While all variability determination was done with the *I*-band observations, *V*-band images were used to characterise the AGN host galaxy colours when available (see Section 7). Table 3 lists the relevant information for the ACS exposures.

3.1 Source Detection and Photometry

The calibrated data for each epoch was obtained from the HST Archive. Typically, a single epoch is comprised of 4 to 6 separate pointings which were combined using the Image Reduction and Analysis Facility (IRAF; PyRAF) tasks MULTIDRIZZLE and TWEAKSHIFTS. The field of view (FOV) for ACS is ~ 5.2 square arcminutes, corresponding to 1.91–2.42 Mpc at redshifts of $z=0.504\text{--}0.888$, and the images were scaled to a resolution of $0''.03$ per pixel. Source Extractor (SExtractor) was used to detect objects in an image created by stacking all available epochs. The catalog was then inspected to remove any spurious detections (i.e. cosmic rays, saturated stars, or objects which fell on the edge of the frame).

The temporal spacing of the epochs for each cluster was approximately a year. We expect most AGN to be variable on these timescales (e.g., Koo et al. 1986; Webb & Malkan 2000; Sesar et al. 2006). Small aperture photometry was performed on each epoch using the PHOT task in PyRAF. Based on the radial profiles of stars and compact galaxies in the fields, $r = 2.5$ is $\sim 2\times$ the FWHM of an unresolved source, which is appropriate for use here as the AGN emission originates from an unresolved nuclear region. A slightly larger aperture of $r = 3.0$ pixels ($0''.09$) was chosen for the photometric catalog to ensure that changes in the PSF would not result in spurious detections of variables (e.g., Sarajedini et al. 2011). We limit our photometric survey to sources with $I_{\text{nuc}} \leq 27$. At magnitudes fainter than this limit, the number counts of sources quickly decline, indicating rapidly increasing incompleteness (Figure 1). We also find that the photometric noise at magnitudes fainter than this limit increases greatly, making variability detection less reliable. This flux limit corresponds to an absolute magnitude of $M_I = -15.25$ at $z = 0.5$ and $M_I = -16.79$ at $z = 0.9$ for the galaxy nuclei.

3.2 Variability Analysis

In order to measure optical variability, the galaxy cluster sample was divided into three groups by exposure time to maximise the total number of sources used to measure the photometric error and determine a threshold for variability. Group 1 consists of those clusters with three epochs of observations and exposure times ~ 3000 s per epoch (MACSJ0257, MACSJ0717, MACSJ0744, MACSJ0911, SDSS1004). Group 2 consists of clusters with two epochs of observations and exposure times ~ 3300 s per epoch (MACSJ1149, MACSJ1423, MACSJ2214). Group 3 consists of clusters with two epochs of observations with exposure times ~ 2100 s per epoch (CL0152, CLJ1226, MS0451, MS1054). In Section 3.3 we describe the method of determining variability for clusters with 2 epochs of ACS observations (Groups 2 and 3), and in Section 3.4 we describe variability determination for clusters with 3 epochs of observations (Group 1).

3.3 Variability with Two Epochs

In the case of clusters with only two epochs of ACS observations, two “fake” epochs were constructed in the same manner as the real epochs. These fake epochs were made by mixing the raw images, taking two from epoch 1 and two from epoch 2 – resulting in two “average” representations of the field with similar noise and depth as the true individual epochs. These images and the resulting photometry carry through the effects of object and sky Poisson noise and readout noise. However, no intrinsic variations should exist and thus the apparent variations in photometry between them can be used to define the noise-magnitude relation upon which we base our variability threshold. Aperture photometry was performed on all sources in both “fake” epochs and the magnitude difference of each object was measured. We then combined the measured magnitude differences of the sources from all clusters in Group 2 and 3 to determine the photometric noise and set a threshold for variability in the real epochs for each group. This approach is the same as that used in Sarajedini et al. (2000) for the Hubble Deep Field.

To quantify photometric noise in our images as a function of magnitude, the magnitude differences were binned and a Gaussian function was fit to the distribution of magnitude differences in each bin. The bin sizes were chosen such that an adequate number of sources fell in each bin for an accurate Gaussian fit. The bin sizes generally spanned a full magnitude in the brighter range (~ 22 – 24) and half a magnitude among fainter objects (~ 24 – 27).

Figure 2 shows an example fit to two magnitude bins for Group 2, illustrating the increased photometric error observed in faint sources compared to bright sources.

We measure the standard deviation of the Gaussian fits to the magnitude difference histograms (called σ hereafter). We then fit a polynomial function to the σ value to produce a smoothly changing variability threshold as a function of magnitude. The magnitude difference of each object was then divided by the value of σ at that magnitude. For a perfect Gaussian distribution, a histogram of these values would be well fit with a Gaussian function having a width or σ of 1 and thus any object showing a change in magnitude greater than 3σ could be identified as varying at 3-sigma significance. We found that the width of the Gaussian fit to $\Delta m/\sigma$ for the photometry of all sources in the fake epochs was generally slightly larger than 1. This value, σ^* , was then adopted as a more conservative variability threshold by defining the threshold as $3.0 \times \sigma \times \sigma^*$, where the value of σ varies with magnitude. Figure 3 illustrates the histogram of $\Delta m/\sigma$ in the fake epochs for all sources in Group 2.

The variability threshold determined using the fake epochs can then be applied to the true time-difference epochs, in which Δmag (i.e. $mag1 - mag2$) was calculated and the objects sorted into bins using the same criteria as that for the fake epochs. Variables were then identified as objects with magnitude differences in the real epochs greater than the variability threshold $3\sigma\sigma^*$. Figures 4 and 5 show the variability plots for all clusters in Groups 2 and 3, and Table 4 lists the optical variables identified in clusters with 2 epochs of HST ACS data and their properties.

3.4 Variability with Three Epochs

In the case where three epochs of ACS data were available (Group 1), variability was determined in a different way, taking advantage of the additional epoch of imaging data. To determine the threshold of variability, the average magnitude and standard deviation were calculated for each object using the photometry from all three epochs. Objects were divided into magnitude bins and a Gaussian function was fit to the values of the standard deviation of the magnitude in each bin. A polynomial function was fit to the histogram central values (i.e., the mean value of the standard deviation as a function of magnitude). We also fit a polynomial to the Gaussian σ values as a function of magnitude. The variability threshold was then defined as the centre of the Gaussian $+ 3 \times \sigma$ (where σ is the standard deviation

of the fit). Thus, an object was defined as variable if the measurement of its magnitude showed a standard deviation above this threshold within its magnitude bin. This approach is similar to that used in Klesman & Sarajedini (2007) and in Sarajedini et al. (2011) for their 5-epoch variability analysis of the GOODS fields. Figure 6 shows the variability plots for all clusters in Group 1, and Table 5 lists the optical variables identified in clusters with 3 epochs of HST ACS data and their properties.

3.5 Summary: Optical Variables in Clusters

We identified two known supernovae among our selected variables from the catalog of Sharon et al. (2010) and removed these, as our aim is to study the AGN population. We find 178 AGN candidates based on the detection of optical variability in our sample of 12 clusters. Ninety (51%) of these variables have greater than 4σ significance. We detect an average of 15 variables per cluster, with a range of 8–24 variables per cluster. We find that 1.1% (178/15,849) of all galaxies in our cluster images are variable down to $I_{nuc} = 27$.

The greatest sources of incompleteness in our variability sample is due to undersampling of the AGN lightcurve with only 2 or 3 epochs of data. Previous variability surveys which have imaged the same field several times over the course of several years (e.g., Trevese et al. 1994; Hawkins 2002) have found that virtually all AGN vary over such a temporal baseline when several epochs of data are analysed. In our survey, we sample only 2 or 3 points on the AGN lightcurve over ~ 1 year, which should result in some incompleteness in our variability survey. In a study of the Hubble Deep Field using 2 epochs of data separated by a few years, Sarajedini et al. (2003) estimate that $\sim 75\%$ of variable AGN would be detected. We expect this same level of completeness in our survey, as we have a similar number of epochs and similar temporal coverage.

False positives or spurious variable sources are also an issue in variability selected samples. To estimate the number of expected spurious sources in our sample, we examine the distribution of variability significance values for all galaxy nuclei in 12 cluster images. Figure 7 shows a histogram of variability significance for all nuclei. The data are well fit by a Gaussian distribution out to a variability significance of 3 and this part of the histogram represents the large number of non-varying galaxy nuclei in our survey. The significant variables, however, appear as a separate population extending to higher significance values. In a normal distribution, we would expect that ~ 48 sources from among our total survey would

have significance values greater than 3. Based on these statistics, we estimate that ~ 30 –40 sources (17–22% of our variables) could be spurious detections.

4 X-RAY DATA REDUCTION AND POINT SOURCE DETECTION

AGN are known to be luminous X-ray sources and can be identified from deep X-ray surveys. Although many previous X-ray surveys for point sources in galaxy clusters have been hindered by the emission of hot intracluster gas, the current generation of X-ray observatories offer the sensitivity, resolution, and positional accuracy needed to detect point sources even in the cores of clusters, and wavelet detection techniques (e.g., Freeman et al. 2002) allow for accurate separation of point source emission from the diffuse background. Thus, the Chandra X-ray Observatory and its supported software package, CIAO, allow us to search for X-ray point sources in the cores of the galaxy clusters in our survey sample.

4.1 Data Reduction

Archival X-ray observations taken with the Chandra X-ray Observatory were obtained from the Chandra Data Archive. Table 6 lists the observation IDs and effective exposure times for each cluster. Data were prepared for analysis using CIAO 4.1.1 and following the steps in the ACIS Data Preparation in the Analysis Guide including afterglow removal, flagging of bad pixels, and removal of background flare events. The observations were filtered by energy into full (0.5–8 keV), hard (2–8 keV), and soft (0.5–2 keV) bands and separate epochs were reprojected and merged into a single observation to obtain the deepest X-ray data possible, resulting in the final effective exposure times listed in Table 6. The data were trimmed to the size of the ACS field of view in order to run source detection on only the area covered by the ACS optical data available for comparison with variability-selected AGN.

4.2 Source Detection

We detected X-ray point sources using the CIAO tool `wavdetect` in the full (0.5–8 keV) band of the merged X-ray images. Source fluxes in the full, hard, and soft bands were calculated using the CIAO tool `eff2evt` in CIAO version 4.3, which calculates the flux in $\text{erg}/\text{cm}^2/\text{s}$ for a specified location on the chip, taking into account the quantum efficiency and effective area.

The flux was measured within a circular aperture created around each source with a

radius equivalent to the source radius determined by `wavdetect`. The background flux at the position of each source was measured using an annulus 2–5 times the size of the source radius, and subsequently subtracted from the source flux. Fluxes were calculated in each band (full, hard, soft) in each individual observation ID; the results were summed to obtain the total source flux, with weighting based on the exposure time of each observation.

For the purpose of comparison with other work, we calculated rest-frame X-ray fluxes assuming a 1D power law plus Galactic absorption model and assumed all X-ray sources to be at the cluster redshift. We used the foreground Galactic extinction toward each cluster from Dickey & Lockman (1990) and assumed a $\Gamma = 1.7$ power law typical of X-ray-selected AGN (e.g., Martini et al. 2006), where Γ is the slope of the power law photon flux density $N_E \propto E^{-\Gamma}$. K-corrections to the observed fluxes were calculated using the `calc_kcorr` function of the Sherpa package in CIAO 4.3. Figure 8 shows the X-ray flux vs. distance from the center of the cluster (defined to be at the position of the Brightest Cluster Galaxy, BCG) as a fraction of the virial radius. While the figure shows both the measured source flux (plus symbols) and the background-subtracted source flux (triangles), only the background-subtracted flux is considered throughout this work. It can be seen that the background subtraction is significant in the inner parts of the clusters, where X-ray emission from hot intracluster gas is significant; the background subtraction is small in the outer parts of the clusters, where the contribution from this gas is minimal. This figure demonstrates our ability to detect X-ray sources down to approximately the same completeness limit in the inner regions of the clusters, where extended cluster X-ray emission is present.

4.3 Summary: X-ray-Detected Sources in Clusters

We find 74 X-ray point sources in our 12 clusters. This is an average of 6 X-ray point sources per cluster with a range of 1–12 per cluster over our entire sample. X-ray point sources in each cluster and their properties are listed in Table 7.

Figure 9 shows a histogram of the X-ray flux in our three bands. We are able to detect sources in the full band to a flux of $\sim 7 \times 10^{-16}$ erg/cm²/s. This flux corresponds to an X-ray luminosity of $\sim 6 \times 10^{40}$ erg/s at a redshift of 0.5 and $\sim 3 \times 10^{42}$ erg/s at a redshift of 0.9. Our survey is thus sensitive to most AGN across the redshift range of our cluster sample. Table 8 lists the parameters used to calculate X-ray luminosities for our point source sample.

We calculate X-ray hardness ratios for objects detected in both the soft (0.5–2 keV), and

hard (2–8 keV) bands. Following the same procedure used for the merged full band images, `wavdetect` was used to analyse the merged soft and hard band images. For objects detected in both bands, we calculate a hardness ratio HR (e.g., Martini et al. 2002):

$$HR = \frac{F_X(2 - 8\text{keV})}{F_X(0.5 - 2\text{keV})} \quad (1)$$

Figure 10 shows the distribution of hardness ratios for the 69 X-ray point sources which are detected in both the hard and soft bands. We find that most sources have HR values on the soft end of the distribution, with 46 sources (67%) having hardness ratios ≤ 5 .

5 INFRARED IMAGE ANALYSIS AND PHOTOMETRY

If dust is present around the AGN, X-ray, UV, and optical emission can be absorbed and re-radiated as infrared light. Galaxies whose emission is dominated by an obscured AGN tend to have mid-IR SEDs which follow a power law ($f_\nu \propto \nu^\alpha$, where α is the spectral index). Donley et al. (2008) find that a power law fit to mid-IR photometry produces a more reliable AGN sample compared to IR colour selected samples or mid-IR excess selection. AGN identified via a power-law fit to the SED in the mid-IR produces a catalog of objects that may not be identified via optical or X-ray emission due to obscuration.

5.1 Data Reduction

Archival Spitzer observations taken with the IRAC (Infrared Array Camera) instrument were available for seven clusters (indicated in Table 1) with exposure times ranging from ~ 900 –6000s. All observations were processed using the IRAC pipeline (version S18.0 or later), and thus corrected BCD (basic calibrated data) files known as cBCD files were available from the Spitzer Science Center. These images were corrected for artefacts such as muxbleed (residual signal in multiplexers), column pulldown (bias shift in columns containing bright sources), banding (bias shift in rows containing bright sources), and first-frame correction (temporal dependence of the bias of each array).

The data were obtained using the Spitzer Pride program Leopard and mosaicked into images for photometry using the MOPEX (MOsaicker and Point source EXtractor) tool which processes calibrated images into a science grade mosaic for point source extraction and photometry. Point source extraction can also be performed with MOPEX, but was in this case performed with Source Extractor in order to incorporate catalogs derived from the optical and X-ray observations.

5.2 Source Identification and Photometry

Source Extractor was used to identify sources and measure the magnitude in each IRAC band, using the $3.6\mu\text{m}$ band as a reference catalog. Photometry was performed with apertures of radius $3''.6$ (6 pixels, or 3 “native” IRAC pixels) and a background annulus from $3''.6 - 8''.4$ (8 pixels, 3–7 “native” IRAC pixels), following the suggestions in the IRAC instrument handbook.¹ The photometric catalog was further refined to include only objects detected in all four IRAC wavebands using the SPHEREMATCH routine in IDL. The flux of each source was calculated by converting the flux from SExtractor (in MJy/sr) to microJy/pix and applying a specified aperture correction from Table 4.7 in version 1.0 (February 2010) of the Spitzer IRAC Instrument Handbook.² The zeropoints to convert flux into Vega magnitudes were obtained from Appendix B (Performing Photometry on IRAC Images) of the Instrument Handbook.

Figure 11 shows a histogram of object magnitudes in each of the IRAC channels. A magnitude of 18 in Channel 4 ($8\mu\text{m}$) corresponds to an IR luminosity of $L_{IR,8\mu\text{m}} = 1.4 \times 10^{42}$ erg/s at a $z = 0.5$ and $L_{IR,8\mu\text{m}} = 6.0 \times 10^{42}$ erg/s at $z = 0.9$. The flux values over all four IRAC channels was fit with a power-law of the form

$$f_\nu \propto \nu^\alpha \quad (2)$$

and minimised χ^2 , selecting galaxies that are well fit ($0.5 < \chi^2_{\text{reduced}} < 1.1$) with a spectral index $\alpha < -0.5$ within 1σ of their errors, following the selection criteria of Alonso-Herrero et al. (2006) for the identification of AGN candidates. This follows from the work of Ivezić et al. (2002), which shows that the spectral indices of optically-selected quasars in the Sloan Digital Sky Survey are in the range of $-0.5 < \alpha < -2$. Alonso-Herrero et al. (2006) also find that the slope of the power law fit relates to the AGN type, where steeper (i.e., more negative) values represent NLAGNs and shallower power law SEDs are classified as BLAGNs.

Figure 12 is an example of one of our mid-IR power law-selected AGN. Table 9 lists the IRAC power law AGN candidates identified in the seven clusters in our study with Spitzer observations along with their properties.

¹ <http://ssc.spitzer.caltech.edu/irac/iracinstrumenthandbook/>

² <http://ssc.spitzer.caltech.edu/irac/iracinstrumenthandbook/home/>

5.3 Summary: IR Power-Law Sources in Clusters

We find 64 sources in our seven clusters with Spitzer observations displaying mid-IR power-law SEDs. This results in an average of 9 IR power-law sources per cluster with a range of 2–18 per cluster. Of our 64 sources, 20 (31%) have slopes steeper than $\alpha = -0.9$ and are similar to the NLAGN SEDs of Alonso-Herrero et al. (2006). The remaining 44 (69%) have shallower slopes and more closely match the BLAGN SED template. We explore the mid-IR colours of these and AGN selected via optical variability and X-ray emission in the following section.

6 MULTI-WAVELENGTH ANALYSIS OF AGN CANDIDATES

The catalogs of X-ray and mid-IR AGN candidates were matched against the optical catalog using the IDL routine SPHEREMATCH with a $2''$ (67 pixels) maximum match radius. While there was generally good alignment between the X-ray and IR data, linear offsets were quantified and applied to the catalogs where needed.

Table 10 lists the IR- and X-ray-selected AGN with optical counterparts in our cluster photometric survey, as well as the number of AGN candidates detected in more than one of the three catalogs. We find that 2/48 (4%) of mid-IR power law sources are detected as optical variables and one of these is variable at $>4\sigma$ confidence. The overlap is greater among the X-ray population, where we find that 12/50 (24%) X-ray point sources are optical variables and two-thirds of these are variable at $>4\sigma$ confidence.

We compare these results to those of Sarajedini et al. (2011) and Klesman & Sarajedini (2007), which examine the properties of AGN candidates identified using similar techniques in the GOODS fields. Both of these studies found that optical variability was observed in about one-quarter of X-ray sources and about half of all mid-IR power-law sources. These percentages do not change considerably when we consider only GOODS field X-ray sources bright enough to be detected in the shallower Chandra observations available for our clusters ($F_X \gtrsim 2 \times 10^{15}$ erg/s/cm² in the full band). Among the X-ray sources detected in our cluster survey, we find that 24% exhibit optical variability, similar to that found in the field population. However, a significantly lower fraction of mid-IR power law sources (4%) are identified as variable in clusters compared to the field.

This inconsistency may be at least partially explained by the different type and temporal sampling of optical data used to determine optical variability in the two surveys. In

the GOODS, variability was measured using *V*-band (F606W) photometric data with 5 epochs covering a 6-month time span. In the cluster analysis, *I*-band (F775W and F814W) photometry was used since multi-epoch imaging was only available at this wavelength. In addition, variability was determined from just 2 or 3 epochs, though generally over a longer time baseline of 1 or 2 years. We expect our variability analysis to be somewhat less sensitive to varying nuclei at this longer wavelength, since it has been shown that optical variability amplitudes increase with decreasing wavelength (Vanden Berk et al. 2004). Based on a comparison of Sarajedini et al. (2000) and Sarajedini et al. (2003), we estimate that about $\sim 50\%$ of *V*-band-detected variables would be identified as variables in our *I*-band survey. Thus, the lower percentage of mid-IR sources identified as variable in our survey may be partially explained by less sensitivity to weakly-varying nuclei in the *I*-band. Indeed, this is seen in Figure 2 of Klesman & Sarajedini (2007), which shows that the variability significance of mid-IR sources is generally quite low, indicating low-level amplitudes of variability. The X-ray sources do not show the same level of sensitivity, which may be due to the fact that they generally display overall greater variability amplitudes (as demonstrated in the large number of $>4\sigma$ confidence variables among this population and also shown in Figure 2 of Klesman & Sarajedini (2007)).

We find that $\sim 7\%$ of variables are also identified as AGN candidates through X-ray emission or mid-IR power law fits. This is less than the fraction of field galaxy variables that are also X-ray/mid-IR sources (36% of GOODS variables after correcting for the X-ray flux level of the cluster survey). This difference may also be due to the lower sensitivity of the *I*-band variability survey in which the light may be more dominated by stars and incompleteness due to the small number of epochs as discussed in Section 3.5.

When comparing our IR and X-ray catalogs, we find that 6/64 (9%) of all IR power law sources are detected as X-ray point sources; when considering only objects with optical counterparts this percentage remains roughly the same (4/48, 8%). Approximately the same percentages are found among X-ray point sources that are also IR power law sources ($\sim 8\%$). The overlap here is less than that found among deeper IR power law source surveys conducted in the GOODS fields (Alonso-Herrero et al. 2006; Donley et al. 2007), where about half of all galaxies displaying power law behaviour across the IRAC channels are also X-ray-detected. Atlee et al. (2011) recently report on a study of low-*z* clusters and find that just $\sim 20\%$ of AGN detected via IR SEDs and/or X-ray emission are identified using both techniques. They hypothesise that the lack of X-ray emission from most of the IR AGNs is due to the larger

column densities of cold gas in the hosts of these galaxies, having found that IR AGN hosts have larger specific star formation rates than the hosts of X-ray AGN. A moderately large column density of cold gas could suppress the X-ray emission from the IR AGNs, making them undetectable in our survey. Additionally, we note that the sensitivity of cluster X-ray surveys may be impeded by the underlying X-ray emitting cluster gas, which could result in some differences in the number of IR AGN detected in X-rays in clusters than in the field.

Figure 13 plots X-ray hardness ratio vs. IR power law slope for the 7 AGN we detect via both methods. Of the AGN we detect in the mid-IR and X-rays, 4/7 have power law indices indicative of BLAGN ($\alpha > -0.9$) and 6/7 have softer X-ray hardness ratios ($HR < 5$). The object with the hardest X-ray flux is also classified with a NLAGN-like mid-IR SED. Both of the objects also detected via optical variability have shallow, BLAGN-like SEDs and are primarily soft X-ray sources. We find no clear correlation between X-ray hardness and mid-IR SED classification, which is consistent with previous studies (e.g., Barmby et al. 2006; Klesman & Sarajedini 2007). Variations in the gas-to-dust ratio or a range of intrinsic AGN properties may explain the reason for the poor correlation between measures of X-ray and IR obscuration, despite the expectation that obscuration should in principle have an effect within both wavelength regimes (Barmby et al. 2006).

Next, we examine the X-ray to optical flux ratios of our X-ray-detected AGN. From our catalog of 74 X-ray point sources, 50 have optical counterparts for which the *I*-band magnitude was measured. We plot the X-ray to optical flux ratio of these sources in Figure 14 with lines of constant $\log(F_X/F_{opt})$. AGN are known to occupy $\log(F_X/F_{opt}) = \pm 1$ (e.g., Comastri et al. 2002; Rigby et al. 2006; Georgakakis et al. 2004). Most (70%) of our X-ray sources lie within this region of the diagram, consistent with the presence of an AGN. Both galaxies we detect via all three AGN detection methods and all galaxies detected in both X-rays and via a mid-IR power law SED are within this range. Of the eight objects detected via both variability and X-rays, 5 (63%) also occupy this region.

High ratios of X-ray to optical flux can indicate the presence of an obscured AGN, even without optical evidence for nuclear activity (e.g., Fiore et al. 2000; Hornschemeier et al. 2001; Giacconi et al. 2001; Barger et al. 2001). Low values indicate X-ray-weak sources that may be optically bright. Objects with $\log(F_X/F_{opt}) \lesssim -2$ are consistent with values of F_X/F_{opt} found in star-forming galaxies (e.g., Moran et al. 1999; Alexander et al. 2002; Bauer et al. 2002; Georgakakis et al. 2003). Georgakakis et al. (2004) finds that objects with F_X/F_{opt} below -2 have optical spectra dominated by the host galaxy, though the presence of a

low-luminosity AGN (LLAGN) cannot be ruled out. X-ray bright optically-normal galaxies (XBONGs) in which the light from the host galaxy dominates the optical spectrum tend to occupy the region $-2 \lesssim \log(F_X/F_{opt}) \lesssim -1$ (Comastri et al. 2002; Rigby et al. 2006). While most of our sources with $\log(F_X/F_{opt}) < -1$ are only detected in X-rays, three AGN candidates are also detected as optical variables, thus increasing the likelihood that they host an AGN and the X-ray emission we detect is due to an accreting supermassive black hole rather than processes related to stars and star formation. Such sources are also found in field AGN surveys (Trevese et al. 2008; Sarajedini et al. 2011).

Finally, we consider the infrared properties of our sample of AGN to determine whether the mid-IR SED is dominated by emission from the AGN or the host galaxy light. Lacy et al. (2004) examine the mid-IR colours of known quasars identified in the Sloan Digital Sky Survey (SDSS) to define a region in colour space for galaxies dominated by an AGN. In Figure 15 we plot our cluster galaxy colours and quantify the numbers of galaxies found in the Lacy wedge in Table 11. We find that 89% of IR power law sources are in the Lacy wedge, along with 16% of optical variables and 44% of X-ray point sources. Conversely, 11% of IR power law sources, 84% of optical variables, and 56% of X-ray point sources are not in the Lacy wedge, and thus we can assume their mid-IR light is dominated by the host galaxy and star formation rather than the AGN. Atlee et al. (2011) find that galaxies in the AGN region of mid-IR colour-colour diagrams must have more than 50% of their mid-IR light contributed by the AGN component. About one quarter of the X-ray and mid-IR selected AGN in their study have colours within the AGN wedge, which is in general agreement with our survey results. This is also consistent with the results of Hickox et al. (2009) for field galaxies, in which they find that 32% of X-ray sources have IR colours within the Stern wedge (Stern et al. 2005). Thus, we find no significant difference between the percentage of X-ray objects with IR colours indicative of AGN emission between the field and cluster population.

In summary, we find that optical variability, X-ray emission, and mid-IR power law SEDs produce a robust catalog of AGN candidates in clusters, with varying degrees of overlap among the samples. Considering AGN detected in all three techniques, we find an average of 25 AGN candidates per cluster with a range of 12–49 per cluster over the survey.

7 DETERMINATION OF CLUSTER GALAXIES

A primary goal of this work is to determine how the cluster environment affects the onset and fuelling of accretion onto a galaxy’s supermassive black hole. In this section we discuss the methods by which we estimate cluster membership for galaxies in each cluster field and compare the percentage of cluster AGN with that found among field studies, as well as examine the effect of cluster physical properties on the AGN fraction.

7.1 Spectroscopic Catalogs

Spectroscopic catalogs of varying completeness are available from the literature for the clusters in our sample. Cluster members were determined using the published redshifts available for each cluster. In the case of the MACS clusters, this range was calculated using the measured velocity dispersion of the cluster galaxies (Barrett 2006) with an average of ~ 40 galaxies per cluster. Table 12 lists the number of sources with published redshifts that fall within the ACS field-of-view, as well as the redshift range spanned by cluster members from the literature. We note that this redshift range is simply the lowest to highest redshift of confirmed cluster members given in the literature and does not fully represent the cluster redshift range.

These catalogs were matched with our photometric catalogs using the IDL routine SPHEREMATCH with a $2''$ (67 pixels) maximum match radius. In some cases a linear offset between the world coordinate systems (WCS) of the ACS images and the spectroscopic catalog was applied. Table 13 lists the AGN candidates in each ACS image having a measured spectroscopic redshift, confirming whether it is a cluster member or field galaxy. A dash indicates that data is not available for this cluster.

7.2 Field Contamination

Each of our cluster fields contains a combination of the galaxy cluster population together with foreground and background galaxies. In order to supplement the existing spectroscopic cluster membership information and better estimate contamination from the field galaxy population, we estimate the number density of the field population in each of our clusters. To do this, we obtained archival HST ACS images of the GOODS-North and GOODS-South fields taken in the F775W filter. Three ACS images near the center of the GOODS-N and GOODS-S fields were selected from the archive with exposure times similar to the depth of

the cluster data: Field 1 (total exposure time 5000s), Field 2 (total exposure time 7028s), and Field 3 (total exposure time 8350s). The data were reduced using the same technique as the cluster ACS images. Images were drizzled to the same resolution ($0''.03/\text{pix}$).

Source extraction and photometry using a Kron flexible elliptical aperture of all galaxies in each tile was performed with Source Extractor. The resulting galaxy photometry catalogs provide an estimate of the mean number of galaxies/arcmin² observed at the depth of our cluster survey:

Field 1 (5000s): 15.6 galaxies/arcmin²

Field 2 (7028s): 16.6 galaxies/arcmin²

Field 3 (8350s): 18.4 galaxies/arcmin²

For each cluster, we now have an estimate of the density of the field galaxy population. We use this to estimate cluster membership probabilities for sources without spectroscopic information as described in the following section.

7.3 Cluster Radial Profiles and Membership Probability

Assuming that the center of each cluster (defined as the Brightest Cluster Galaxy) contains the highest concentration of cluster galaxies with a decreasing contribution from the galaxy cluster and increasing contribution from the field with increasing distance from the center, we calculate the number of galaxies/arcmin² vs. radius in bins of varying size from 0.3–0.01 arcmin starting from the center of each cluster. We then assume at each radius a constant density for the field population as determined in Section 7.2. By subtracting the field density, a field-decontaminated density profile of the cluster can be produced. An example of the galaxy density as a function of cluster radius is shown in the top panel of Figure 16 for CLJ1226. The average value of the galaxy density of the field is also shown, as well as the field-subtracted radial profile of the cluster.

At any given radius, the total number of galaxies (T) is equal to the number of galaxies in the field (F) plus the number of galaxies in the cluster (C). Therefore, $T = F + C$ and by subtracting the field from the total, we estimated the number of galaxies in the cluster (C) at any given radius. From this, we calculate the percentage of galaxies at each radius in the cluster and the field.

$$\% \text{ galaxies in the field} = F/T \quad (3)$$

$$\% \text{ galaxies in the cluster} = C/T \quad (4)$$

The resulting values were fit with a polynomial to model the radial probability profile of each cluster. We then determine the probability from 0 (not in the cluster) to 1 (in the cluster) for each galaxy in our image based on its distance from the center of the cluster. An example is shown in the bottom panel of Figure 16. Based on these radial probability profiles, each galaxy is assigned a weight equal to its cluster membership likelihood. Galaxies with spectroscopic data are assigned a weight of 1 or 0 based on whether their spectroscopic redshift lies within the range of cluster redshift values given in Table 12.

7.4 Colour Selection and Cluster Membership Probability

In addition to using radial distance in the cluster to determine probability of cluster membership, we also use galaxy colour to increase cluster membership probability for galaxies with colours matching those of known cluster members at the cluster redshift. The galaxy cluster sample can be roughly divided into three redshift bins at $z = 0.5$, 0.7 , and 0.85 . For each of the three redshift groups, we examined the $V-I$ colours for the cluster with the most spectroscopically-confirmed cluster members (MACSJ0717 at $z \sim 0.5$, MACSJ0744 at $z \sim 0.7$, and MS1054 at $z \sim 0.85$) and compared the peak of the cluster member galaxy colour distribution with the expected galaxy colours for early type galaxies (E/S0) at these redshifts in Fukugita et al. (1995). The observed peak in $V-I$ (F555W-F814W) colours of cluster members galaxies in MACSJ0717 is 2.54, which very closely matches the expected galaxy colour of $V-I = 2.48$ given in Fukugita et al. (1995) for early type galaxies.

In the case of MS1054, the $V-I$ colour we have available is F606W-F775W, which cannot be directly compared with Fukugita et al. (1995), where colours are provided in different filters. We therefore use the published values of Tran et al. (2007), who find a mean colour of F606W-F775W = 1.61 for red, bright elliptical galaxies in MS1054. This is consistent with the value of 1.69 that we measure for the cluster members. Fukugita et al. (1995) does not provide galaxy colours at a redshift of 0.7 so a linear extrapolation was fit to the expected $V-I$ galaxy colours for elliptical galaxies between a redshift of 0.5 and 0.8. The value of 2.79 we obtain from this fit is consistent with the observed peak value of 2.66 for cluster members in MACSJ0744.

Figure 17 shows the $V-I$ galaxy colour distributions for spectroscopically-confirmed clus-

ter members (solid line), non-cluster members (dotted line), and all galaxies in the cluster image (dashed line) for MACSJ0717, MACSJ0744, and MS1054. Based on the colour distribution of cluster members, we estimate that all galaxies with colours redder than the blue end of this distribution have a high probability of residing in the cluster. We determine the $V-I$ colour threshold to be $F555W-F814W = 2.36$ for clusters at redshift $z \sim 0.5$, $F555W-F814W = 2.43$ for clusters at redshift $z \sim 0.7$, and $F606W-F775W = 1.49$ for clusters at redshift $z \sim 0.85$ based on the colour distribution for cluster members in these three representative clusters. In order to determine the probability that should be assigned to galaxies redder than this limit, we examined the radial profiles of cluster members in all clusters and determined the average value of their radially-determined cluster membership probability. This was generally found to be $\sim 80\%$ for all clusters. We therefore increase the cluster membership probability to 80% for galaxies redder than the colour thresholds determined here. If a red galaxy had already been assigned a cluster membership probability higher than 80%, it retained the higher probability value. Figure 18 shows an example of galaxy cluster membership probability values for the cluster MACSJ0717.

Because the population of confirmed cluster members in these clusters consist of mainly red, early type galaxies, we could not determine a colour-based probability for blue galaxies. Thus, while bluer galaxies did not receive decreased membership probability values, their probabilities are based solely on their radial distance from the center of the cluster or spectroscopic information when available, as statistical information about the blue galaxy population is not easily determined.

8 PERCENTAGE OF AGN IN CLUSTERS

To determine the percentage of AGN in clusters, we divide the total number of AGN in each cluster by the total number of galaxies in the cluster. First, we compute the percentage for spectroscopically-confirmed cluster members only (where SC stands for "spectroscopically confirmed"):

$$\% \text{ AGN}_{\text{spec}} = \frac{\# \text{ SC cluster AGN}}{\# \text{ SC cluster galaxies}} \quad (5)$$

Since spectroscopic coverage varies from cluster to cluster and is sometimes sparse, we also calculate an AGN percentage using all sources in the ACS FOV for each cluster, which covers roughly half of the virial radius. We call this the non-weighted AGN percentage. Finally, we compute our weighted AGN percentage using the cluster membership probabilities described

in Sections 7.3 and 7.4 based on radial distance and colour information (where CMP stands for "cluster membership probability):

$$\% \text{ AGN}_{\text{weighted}} = \frac{\sum(\text{AGN CMP})}{\sum(\text{galaxy CMP})} \quad (6)$$

Table 14 lists the weighted and non-weighted total percentages of AGN in our galaxy clusters as well as the percentage of AGN detected among spectroscopically-confirmed cluster members. We find that our clusters have a range of 0.8–3.75% AGN (weighted), with a median value of $2.27 \pm 1.5\%$. If we consider confirmed cluster members only, we find that for the 11 clusters with redshift information, 25/530 or 4.7% of confirmed cluster members show evidence of nuclear activity. Table 15 lists the percentage of cluster AGN detected using each of the 3 techniques. In both Table 14 and Table 15, a dash (-) indicates that data is not available while an x indicates there are no AGN detected, though data exist.

We observe that the fraction of AGN among spectroscopically-confirmed cluster galaxies is systematically higher than the fraction observed among field-corrected galaxies. This discrepancy can be resolved by noting that the probability of hosting an AGN increases with host galaxy brightness (e.g., Ho et al. 1997; Sarajedini et al. 2003), as well as the fact that any contribution from the AGN's luminosity may serve to increase its host galaxy's brightness. Given that the brightest cluster galaxies are systematically chosen for redshift observations because of their luminosity, we expect to see an increase in the AGN percentage among spectroscopically-confirmed cluster members versus our field-corrected cluster members. We will show in Section 8.1 that when we impose a magnitude limit on our sample, we also observe a higher percentage of AGN. Sarajedini et al. (2011) observe a similar result, as illustrated in their Figure 9 showing that the fraction of galaxies hosting AGN increases with host galaxy luminosity.

8.1 Comparison with Field AGN Surveys

In Sarajedini et al. (2011), AGN candidates were identified in the GOODS fields using the same identification techniques as those used in this study. They identified 85 optically varying galaxies, 259 X-ray sources, and 22 IR power-law sources in these fields. To compare with our cluster survey, we impose several flux limits to the different survey samples. We consider only the sixty-eight X-ray sources in GOODS detectable down to a limit of $\sim 2 \times 10^{-15}$ erg/cm²/s, similar to the average depth reached in the X-ray observations of our cluster sample. We further limit the field sample to the redshift range of our clusters ($z = 0.4\text{--}0.9$). With these

restrictions, we find 31/1235 galaxies in the GOODS fields host AGN ($2.5 \pm 1.6\%$). This is comparable to, though slightly higher than, the median weighted value we find of $2.27 \pm 1.5\%$ in clusters. If we further limit our cluster sample to only the 7 in which all 3 AGN selection criteria are possible (i.e., those with mid-IR observations), the AGN percentage is $2.5 \pm 1.6\%$, exactly equal to the field AGN percentage.

It is also necessary to ensure that the galaxy magnitude distributions of the GOODS fields and our cluster galaxies are comparable. Since the GOODS survey individual epoch images are shallower than our cluster images (1000s, compared with 2100–3000s), the variability analysis in the GOODS fields extends only to ~ 24.5 , while our cluster photometry extends to $I \sim 26$. We therefore impose a galaxy magnitude limit of $I = 24.5$ on all objects in our cluster sample to further match the GOODS sample. This results in a median weighted AGN percentage among all our clusters of 4.01%, which rises to $4.94 \pm 2.2\%$ if we consider only those clusters with IR observations (and thus all three AGN selection techniques are possible). With only the number of known cluster members in these seven clusters, the AGN percentage is $5.5 \pm 2.3\%$ (20/363). These findings indicate that the number of AGN among galaxies in clusters ($\sim 5\%$) is similar or slightly greater than that in the field ($\sim 2.5\%$), though only at $\sim 1\sigma$ significance.

8.2 Comparison with Cluster X-ray Surveys for AGN

Martini et al. (2002) found a lower limit of $\sim 5\%$ AGN in the cluster A2104 ($z = 0.154$) with optical counterparts down to an absolute magnitude of $R < 20$. This corresponds to six X-ray-detected AGN, only one of which shows optical emission lines in its spectra indicative of AGN activity. This is consistent with emission line surveys such as Dressler et al. (1999), and suggests that the fraction of AGN in clusters may be higher than previously determined if additional AGN detection techniques are employed.

Martini et al. (2009) conducted a survey of the luminous AGN population in clusters out to $z = 1.3$. Their sample includes two of our clusters, MS0451 and MS1054. They required that their sources 1) must have a hard X-ray luminosity $L_{X,H} \geq 10^{43}$ erg/s, 2) the redshift must be within 3 times the cluster’s velocity dispersion of the cluster redshift, 3) the source must lie within the projected virial radius of the cluster, and 4) the absolute magnitude of the host galaxy must be $M_R = M^*(z) + 1$. They detect no X-ray AGN in MS0451 meeting this criteria, and when these criteria are applied to our X-ray sources in that cluster, we

come to the same result. Martini et al. (2009) detect one X-ray point source meeting their requirements in the cluster MS1054, but it falls outside of our ACS FOV and therefore was not included in our survey. We also do not detect any other X-ray sources within the ACS FOV that meet these criteria.

We also compare our results with the X-ray source catalog of Johnson et al. (2003), in which the authors identify 47 X-ray point sources in MS1054 down to fluxes similar to those achieved in our data. They find a $\sim 2\sigma$ excess of X-ray point sources in this particular cluster down to an X-ray flux of 5×10^{-15} erg/s/cm², which is consistent with an excess of ~ 6 AGNs relative to the field. Their survey area is 8.3×8.3 arcmin², a factor of 2.5 times larger than the area used in our variability survey per cluster field. Seven of the sources found in Johnson et al. (2003) fall within our survey FOV and we detect six of these sources, thus confirming their result.

8.3 Cluster Properties

Finally, we investigate whether cluster properties such as redshift, mass, luminosity, velocity dispersion, virial radius, and morphology have any impact on the percentage of AGN. Galametz et al. (2009) and Martini et al. (2009) both find evidence for an increase in the number of AGN in clusters with redshift. Figure 19 shows the total weighted percentage of AGN in our clusters as a function of cluster redshift. Over the redshift range of our survey, $z = 0.5\text{--}0.9$, the percentage of AGN appears to be constant. The percentages of variables, X-ray point sources, and IR power-law sources also remain roughly constant regardless of cluster redshift. These results are not inconsistent with the findings of previous studies, as the redshift range covered by our clusters is slightly narrower than that of these studies. This figure suggests that we reach similar levels of completeness in detecting AGN over the redshift range of our cluster sample.

The cluster X-ray luminosity comes from thermal bremsstrahlung emission from hot ($T \sim 10^8$ K) intracluster gas bound to the gravitational potential and is therefore related to the cluster mass. As shown in Figure 20, there appears to be no change in the total weighted percentage of AGN with the cluster's X-ray luminosity. There also appears to be no significant correlation between the percentage of optical variables, IR power law sources, or X-ray point sources with the X-ray luminosity of the cluster. Thus, the fraction of AGN

among galaxies in clusters does not appear to depend on hot gas content over the range sampled by our survey clusters.

In Figure 21 we investigate correlations between the percentage of AGN and the cluster size measured by its virial radius. Though our clusters cover a large range of virial radii, from ~ 1.1 – 2.6 Mpc, the total percentage of AGN detected in the clusters remains roughly constant over this range. This is also the case for the optical variables and the X-ray point sources, though the IR power law sources reveal a very slight decline in the percentage of IR sources detected as a function of cluster virial radius. Additionally, we observe no trend between AGN percentage and cluster virial mass, which is not surprising given the correlation between virial mass and virial radius.

In Figure 22, we look at the percentage of AGN versus the cluster velocity dispersion. There appears to be no significant correlation between the total percentage of AGN and the cluster velocity dispersion, even over our range of 600–1800 km/s. This is also true for optical variables and X-ray point sources, though the IR power law sources show a slight increase in the AGN fraction with increasing velocity dispersion.

Ebeling et al. (2007) assigns each of the MACS clusters in our sample a morphology code, dependent on the agreement between the X-ray and optical emission in the cluster, as well as signs of disturbances in the cluster substructure. Their morphology codes are assigned based on the following criteria:

- 1: Relaxed (pronounced cool core, perfect alignment of X-ray peak and single cD galaxy)
- 2: Semi-Relaxed (good optical/X-ray alignment, concentric contours)
- 3: Semi-Disturbed (nonconcentric contours, obvious small-scale substructure)
- 4: Disturbed (poor optical/X-ray alignment, multiple peaks, no cD galaxy)

Based on these definitions, they gave the galaxy clusters that appear in our sample the following morphology classifications:

MACSJ0257: 2 (Semi-Relaxed)

MACSJ0717: 4 (Disturbed)

MACSJ0744: 2 (Semi-Relaxed)

MACSJ0911: 4 (Disturbed)

MACSJ1149: 4 (Disturbed)

MACSJ1423: 1 (Relaxed)

MACSJ2214: 2 (Semi-Relaxed)

Using the classification criteria of Ebeling et al. (2007), we assign a morphology code to each of our remaining clusters:

CL0152: 4 (Disturbed)

CLJ1226: 1 (Relaxed)

MS0451: 1 (Relaxed)

MS1054: 3 (Semi-Disturbed)

SDSS1004: 1 (Relaxed)

With only a small number of clusters in each of these morphological groups, we combine the relaxed and semi-relaxed clusters (7 clusters), and also the disturbed and semi-disturbed clusters (5 clusters). A comparison of the median value of the weighted percentage of AGN shows that both groups have very similar percentages of AGN: the relaxed clusters have a median value of 2.13% and the disturbed clusters have a median value of 2.27%. If we exclude clusters with no IR observations, we have 3 clusters in the disturbed group and 4 clusters in the relaxed group. We find that the disturbed clusters have a median percentage of 2.29% cluster AGN, while the relaxed clusters have a median AGN percentage of 3.13%. Thus, we do not find evidence that the cluster dynamical state has an impact on the number of AGN detected in our sample of clusters.

8.4 Summary: AGN Percentage

Comparing our results with the multi-wavelength GOODS AGN field survey of Sarajedini et al. (2011), we find that the percentage of AGN is similar to or slightly enhanced in clusters relative to the field when considering AGN identified via optical variability, X-ray emission, or mid-IR power-law SEDs. We also find that the number of X-ray-detected AGN in our survey is consistent with other surveys for X-ray point sources in galaxy clusters, which have reported an enhancement of X-ray sources among some galaxy clusters relative to the field. These two findings may at first appear to be inconsistent. Are the number of AGN in clusters more than or the same as that found in the field? The answer seems to depend

strongly on completeness issues and correcting for galaxy magnitude limits as well as X-ray flux limits in the surveys being compared. In any case, it seems clear that AGN activity is in no way inhibited in the cluster environment.

This is evidence that galaxies are still able to fuel accretion onto their supermassive black holes, even in denser environments. Martini et al. (2004) point out that while major mergers may be perhaps the only reasonable candidate to trigger and sustain luminous AGN, lower luminosity AGN such as those identified by our survey may have significantly more physical processes capable of fuelling a central supermassive black hole, including bar structures, minor mergers, galaxy harassment, and stellar mass loss – all of which still play a significant role in a galaxy cluster environment. If this is in fact the case, there may be a comparable number of lower luminosity AGN in clusters and in the field, which is consistent with our results, as optical variability and IR power law detection are likely to pick out lower luminosity AGN. This is also consistent with the picture that more luminous AGN may be less common in denser environments (e.g., Kauffmann et al. 2004; Popesso & Biviano 2006), as we find no luminous X-ray sources in MS0451 or MS1054, consistent with the survey of Martini et al. (2009).

We find no obvious trends between the AGN fraction in clusters and various cluster properties, including mass, X-ray luminosity, virial radius, velocity dispersion, redshift and morphology. We do note that many of these properties are interrelated, and in general the clusters in our sample cover a small range of mass and X-ray luminosity. We find that the number of AGN we detect is roughly constant regardless of redshift, confirming that we are able to reach similar levels of completeness over the range of cluster redshifts in our sample. Finally, we do not observe a significant link between cluster morphology and the number of AGN we detect, finding similar percentages of cluster AGN in both disturbed and relaxed clusters.

9 CONCLUSIONS

We have explored several issues concerning the AGN population in dense cluster environments. We analysed 12 galaxy clusters at redshifts $0.5 < z < 0.9$ to determine the AGN fraction and address the issue of AGN fuelling in massive galaxy clusters. We compile, for the first time, a catalog of cluster AGN candidates using a combination of three detection techniques: optical variability, X-ray point source detection, and mid-IR power-law SEDs.

We identify 178 optical variables among the galaxies in our cluster sample using 2–3 epochs of ACS imaging, an average of 15 variables per cluster. Ninety (51%) of these variables have $>4\sigma$ significance. We find that in total, 1.1% of all galaxies surveyed display nuclear optical variability in galaxies to $I_{nuc} = 27$, corresponding to an absolute magnitude of $M_I \sim -15.3$ at a redshift of 0.5 and $M_I \sim -16.8$ at a redshift of 0.9.

We find 74 X-ray point sources down to a full band flux of $\sim 7 \times 10^{-16}$ erg/cm²/s using Chandra X-ray imaging, an average of 6 X-ray point sources per cluster. This flux corresponds to an X-ray luminosity of $\sim 6 \times 10^{40}$ erg/s at a redshift of 0.5 and $\sim 3 \times 10^{42}$ erg/s at a redshift of 0.9. Most of the point sources have hardness ratios on the soft end of the distribution, with 46 sources (67%) having $F_X(2-8 \text{ keV})/F_X(0.5-2 \text{ keV}) \leq 5$. Seventy percent of our X-ray sources lie within $\log(F_X/F_{opt}) = \pm 1$, consistent with the presence of an AGN.

Spitzer IRAC data is available for 7 clusters, in which we identify a total of 64 IR power law sources. This is an average of 9 IR power law sources per cluster. Of these objects, 44% show BLAGN-like mid-IR SEDs, while 31% have steeper, NLAGN-like SEDs. We find that 87–100% of IR power law sources are in the Lacy AGN wedge, while 13–16% of optical variables and 38–47% of X-ray point sources lie in the Lacy wedge. This indicates that the majority of optically variable AGN and about half of X-ray-selected AGN are not dominated by the AGN light in the mid-IR.

In total, we find an average of 25 AGN candidates per cluster with a range of 12–49 per cluster over the sample. We identify 50 X-ray point sources and 48 mid-IR power law sources with optical counterparts, and find that 4% of mid-IR power law sources and 24% of X-ray point sources are detected as optical variables. Only seven percent of variables are also detected either through X-ray emission or as mid-IR power law sources. Among the X-ray and IR objects we find that 9% of IR power law sources are also detected via X-rays, while 8% of X-ray point sources also show a power law SED in the mid-IR.

A primary goal of our work is to calculate the percentage of cluster AGN, taking into account the cluster membership probability for each galaxy. We find that our clusters have a range of $\sim 1-4\%$ AGN with a median value of $2.3 \pm 1.5\%$. We compare the percentage of cluster AGN with the percentage of AGN among field galaxies in the GOODS field detected via optical variability, X-rays, or mid-IR SED fitting. Within the same redshift and X-ray flux limits as our cluster data, $2.5 \pm 1.6\%$ of field galaxies are found to host AGN. Applying a galaxy magnitude limit to our cluster data to match the shallower exposure times in GOODS, we find a median weighted AGN percentage among the clusters of $4.94 \pm 2.2\%$.

Thus, we find that the number of AGN among galaxies in clusters is essentially the same as that in the field. We find no obvious trends among cluster properties and the percentage of AGN detected, though in most cases our clusters cover a relatively small range of these properties. We also do not find a significant difference in the percentage of cluster galaxies that host AGN as a function of cluster dynamical state or morphology.

Our results confirm earlier indications that galaxies are able to fuel accretion onto the central supermassive black hole even in denser cluster environments. While major mergers may be a strong candidate to trigger and sustain luminous AGN, lower luminosity AGN, such as many of those identified by our survey, may be triggered or sustained through a greater variety of physical processes including bar structures, minor mergers, galaxy harassment, and stellar mass loss – all of which still play a significant role in the cluster environment.

In a future paper we will present the radial distribution of AGN among cluster galaxies to examine how local environment affects the spatial distribution of AGN within the cluster. We will also explore the properties of the AGN host galaxies in our survey to investigate the link between AGN activity and the evolution of galaxies. Using our sample, we will examine the relationship between the presence of an AGN, the host galaxy, and the cluster environment.

REFERENCES

- Abell G. O., 1965, *ARA&A*, 3, 1
- Alexander D. M., Aussel H., Bauer F. E., Brandt W. N., Hornschemeier A. E., Vignali C., Garmire G. P., Schneider D. P., 2002, *ApJ*, 568, L85
- Alonso-Herrero A. et al., 2006, *ApJ*, 640, 167
- Atlee D. W., Martini P., Assef R. J., Kelson D. D., Mulchaey J. S., 2011, *ApJ*, 729, 22
- Barger A. J., Cowie L. L., Mushotzky R. F., Richards E. A., 2001, *AJ*, 121, 662
- Barmby P. et al., 2006, *ApJ*, 642, 126
- Barrett E., 2006, PhD thesis, University of Hawai'i at Manoa
- Bauer F. E., Alexander D. M., Brandt W. N., Hornschemeier A. E., Vignali C., Garmire G. P., Schneider D. P., 2002, *AJ*, 124, 2351
- Comastri A. et al., 2002, *ArXiv Astrophysics e-prints*
- Demarco R. et al., 2005, *A&A*, 432, 381
- Dickey J. M., Lockman F. J., 1990, *ARAA*, 28, 215

- Donahue M., Gaskin J. A., Patel S. K., Joy M., Clowe D., Hughes J. P., 2003, *ApJ*, 598, 190
- Donley J. L., Rieke G. H., Pérez-González P. G., Barro G., 2008, *ApJ*, 687, 111
- Donley J. L., Rieke G. H., Pérez-González P. G., Rigby J. R., Alonso-Herrero A., 2007, *ApJ*, 660, 167
- Dressler A., Smail I., Poggianti B. M., Butcher H., Couch W. J., Ellis R. S., Oemler, Jr. A., 1999, *ApJS*, 122, 51
- Dressler A., Thompson I. B., Shectman S. A., 1985, *ApJ*, 288, 481
- Ebeling H., Barrett E., Donovan D., Ma C.-J., Edge A. C., van Speybroeck L., 2007, *ApJL*, 661, L33
- Ebeling H., Edge A. C., Henry J. P., 2001, *ApJ*, 553, 668
- Ebeling H. et al., 2000, *ApJ*, 534, 133
- Ellis S. C., Jones L. R., Donovan D., Ebeling H., Khosroshahi H. G., 2006, *MNRAS*, 368, 769
- Ferrarese L., Merritt D., 2000, *ApJL*, 539, L9
- Fiore F. et al., 2000, *New Astronomy*, 5, 143
- Freeman P. E., Kashyap V., Rosner R., Lamb D. Q., 2002, *ApJS*, 138, 185
- Fukugita M., Shimasaku K., Ichikawa T., 1995, *PASP*, 107, 945
- Galametz A. et al., 2009, *ApJ*, 694, 1309
- Gebhardt K. et al., 2000, *ApJL*, 539, L13
- Georgakakis A. et al., 2004, *MNRAS*, 349, 135
- Georgakakis A., Hopkins A. M., Sullivan M., Afonso J., Georgantopoulos I., Mobasher B., Cram L. E., 2003, *MNRAS*, 345, 939
- Giacconi R. et al., 2001, *ApJ*, 551, 624
- Gisler G. R., 1978, *MNRAS*, 183, 633
- Hawkins M. R. S., 2002, *MNRAS*, 329, 76
- Hickox R. C. et al., 2009, *ApJ*, 696, 891
- Ho L. C., Filippenko A. V., Sargent W. L. W., 1997, *ApJS*, 112, 315
- Hoekstra H., Franx M., Kuijken K., 2000, *ApJ*, 532, 88
- Hornschemeier A. E. et al., 2001, *ApJ*, 554, 742
- Hubble E., Humason M. L., 1931, *ApJ*, 74, 43
- Inada N. et al., 2005, *Astronomical Society Japan Publications*, 57, L7
- Inada N. et al., 2003, *Nature*, 426, 810

- Ivezić Ž. et al., 2002, *AJ*, 124, 2364
- Jee M. J., White R. L., Benítez N., Ford H. C., Blakeslee J. P., Rosati P., Demarco R., Illingworth G. D., 2005a, *ApJ*, 618, 46
- Jee M. J., White R. L., Ford H. C., Blakeslee J. P., Illingworth G. D., Coe D. A., Tran K., 2005b, *ApJ*, 634, 813
- Johnson O., Best P. N., Almaini O., 2003, *MNRAS*, 343, 924
- Kauffmann G., White S. D. M., Heckman T. M., Ménard B., Brinchmann J., Charlot S., Tremonti C., Brinkmann J., 2004, *MNRAS*, 353, 713
- Klesman A., Sarajedini V., 2007, *ApJ*, 665, 225
- Koo D. C., Kron R. G., Cudworth K. M., 1986, *PASP*, 98, 285
- Kormendy J., Richstone D., 1995, *ARAA*, 33, 581
- Lacy M., Petric A. O., Sajina A., Canalizo G., Storrie-Lombardi L. J., Armus L., Fadda D., Marleau F. R., 2007, *AJ*, 133, 186
- Lacy M. et al., 2004, *ApJS*, 154, 166
- Limousin M. et al., 2010, *MNRAS*, 405, 777
- Lynden-Bell D., 1969, *Nature*, 223, 690
- Magorrian J. et al., 1998, *AJ*, 115, 2285
- Makino J., Hut P., 1997, *ApJ*, 481, 83
- Martini P., Kelson D. D., Kim E., Mulchaey J. S., Athey A. A., 2006, *ApJ*, 644, 116
- Martini P., Kelson D. D., Mulchaey J. S., Athey A., 2004, *Clusters of Galaxies: Probes of Cosmological Structure and Galaxy Evolution*
- Martini P., Kelson D. D., Mulchaey J. S., Trager S. C., 2002, *ApJL*, 576, L109
- Martini P., Sivakoff G. R., Mulchaey J. S., 2009, *ApJ*, 701, 66
- Maughan B. J., Jones C., Jones L. R., Van Speybroeck L., 2007, *ApJ*, 659, 1125
- Maughan B. J., Jones L. R., Ebeling H., Perlman E., Rosati P., Frye C., Mullis C. R., 2003, *ApJ*, 587, 589
- Maughan B. J., Jones L. R., Ebeling H., Scharf C., 2004, *MNRAS*, 351, 1193
- McLeod K. K., Bechtold J., 2010, in *Bulletin of the American Astronomical Society*, Vol. 42, American Astronomical Society Meeting Abstracts #215, p. 371
- Molnar S. M., Hughes J. P., Donahue M., Joy M., 2002, *ApJL*, 573, L91
- Moran E. C., Lehnert M. D., Helfand D. J., 1999, *ApJ*, 526, 649
- Moran S. M., Ellis R. S., Treu T., Smith G. P., Rich R. M., Smail I., 2007, *ApJ*, 671, 1503

- Morgan W. W., 1961, Proceedings of the National Academy of Science, 47, 905
- Oemler, Jr. A., 1974, ApJ, 194, 1
- Oguri M., 2010, PASJ, 62, 1017
- Peterson B. M., 2001, in Advanced Lectures on the Starburst-AGN, I. Aretxaga, D. Kunth, & R. Mújica, ed., pp. 3–+
- Popesso P., Biviano A., 2006, A&A, 460, L23
- Reiprich T. H., Böhringer H., 2002, ApJ, 567, 716
- Rigby J. R., Rieke G. H., Donley J. L., Alonso-Herrero A., Pérez-González P. G., 2006, ApJ, 645, 115
- Rines K., Geller M. J., Kurtz M. J., Diaferio A., 2003, AJ, 126, 2152
- Salpeter E. E., 1964, ApJ, 140, 796
- Sarajedini V. L., Gilliland R. L., Kasm C., 2003, ApJ, 599, 173
- Sarajedini V. L., Gilliland R. L., Phillips M. M., 2000, AJ, 120, 2825
- Sarajedini V. L., Koo D. C., Klesman A. J., Laird E. S., Perez Gonzalez P. G., Mozena M., 2011, ApJ, 731, 97
- Sarajedini V. L. et al., 2006, ApJS, 166, 69
- Sesar B. et al., 2006, AJ, 131, 2801
- Sharon K. et al., 2010, ApJ, 718, 876
- Stern D. et al., 2005, ApJ, 631, 163
- Stott J. P., Smail I., Edge A. C., Ebeling H., Smith G. P., Kneib J., Pimbblet K. A., 2007, ApJ, 661, 95
- Sunyaev R. A., Titarchuk L. G., 1980, A&A, 86, 121
- Tran K., Franx M., Illingworth G. D., van Dokkum P., Kelson D. D., Blakeslee J. P., Postman M., 2007, ApJ, 661, 750
- Tran K., Kelson D. D., van Dokkum P., Franx M., Illingworth G. D., Magee D., 1999, ApJ, 522, 39
- Trevese D., Boutsia K., Vagnetti F., Cappellaro E., Puccetti S., 2008, A&A, 488, 73
- Trevese D., Kron R. G., Majewski S. R., Bershadsky M. A., Koo D. C., 1994, ApJ, 433, 494
- van Dokkum P. G., Franx M., Fabricant D., Illingworth G. D., Kelson D. D., 2000, ApJ, 541, 95
- Vanden Berk D. E. et al., 2004, ApJ, 601, 692
- Webb W., Malkan M., 2000, APJ, 540, 652
- Williams L. L. R., Saha P., 2004, AJ, 128, 2631

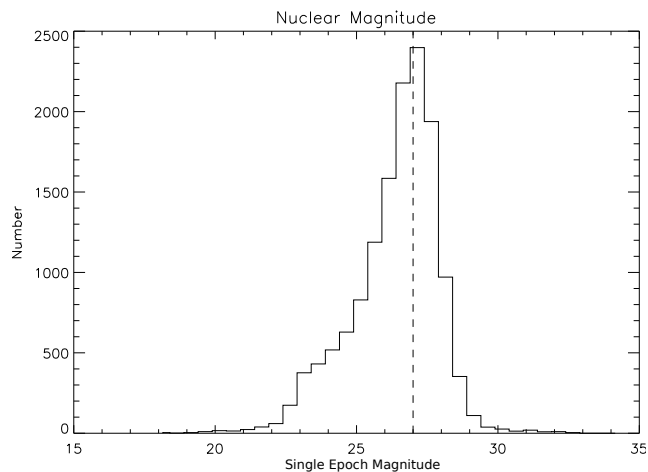


Figure 1. Histogram of nuclear magnitude (I -band) in a single epoch for all galaxies in the cluster sample. The magnitude limit is indicated by the vertical dashed line.

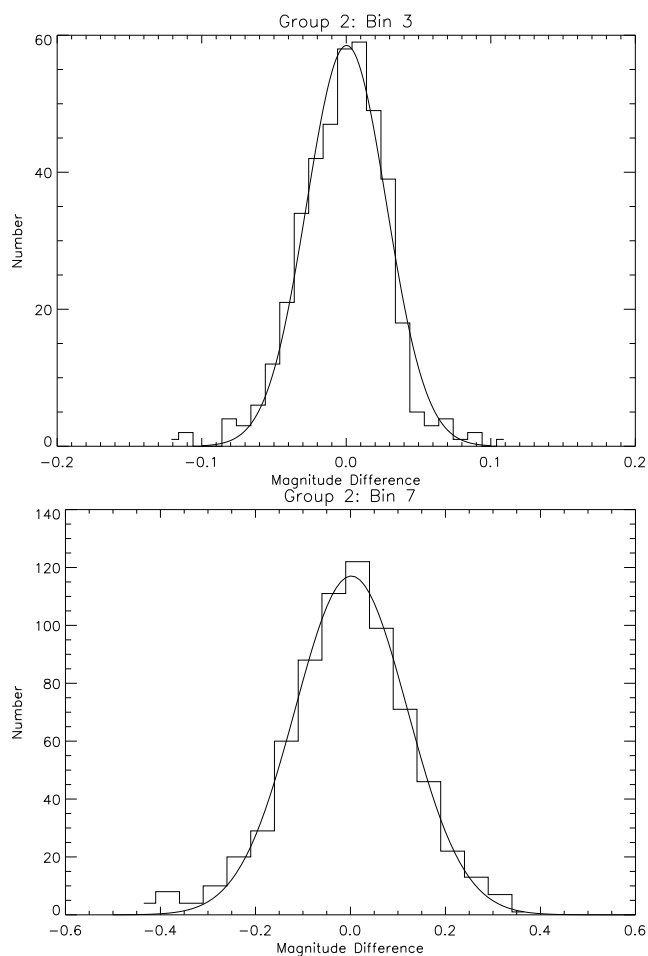


Figure 2. Gaussian fits to the histogram of magnitude differences in two magnitude bins for Group 2. Bin 3 (top) is the difference in magnitudes for objects between $I = 24.5$ – 25.5 and Bin 7 (bottom) is the difference in magnitude for objects with magnitudes between $I = 27$ – 27.5 . The width of this Gaussians plotted here, σ , are used to calculate the variability threshold for sources in that magnitude bin.

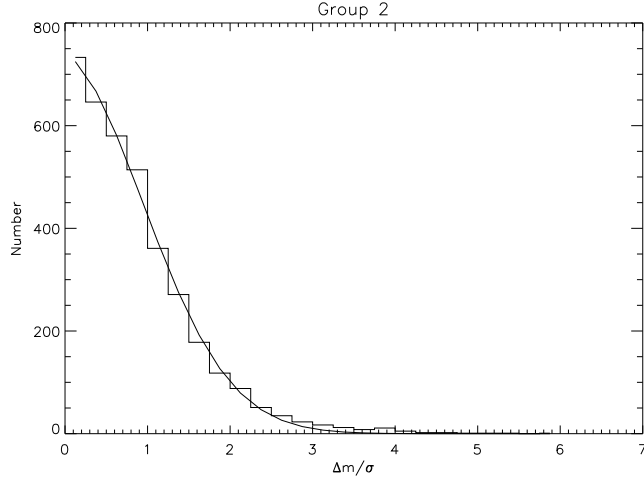


Figure 3. Gaussian fit to assess the photometric noise in the fake epochs in Group 2. The value of "width" for this fit is 1.06 (this is σ^*). Thus any " 3σ -confidence" variability detection must actually display magnitude variations of 3.18 times the σ value determined at its magnitude. The fit for Group 3 was found to have a value for σ^* of 1.07.

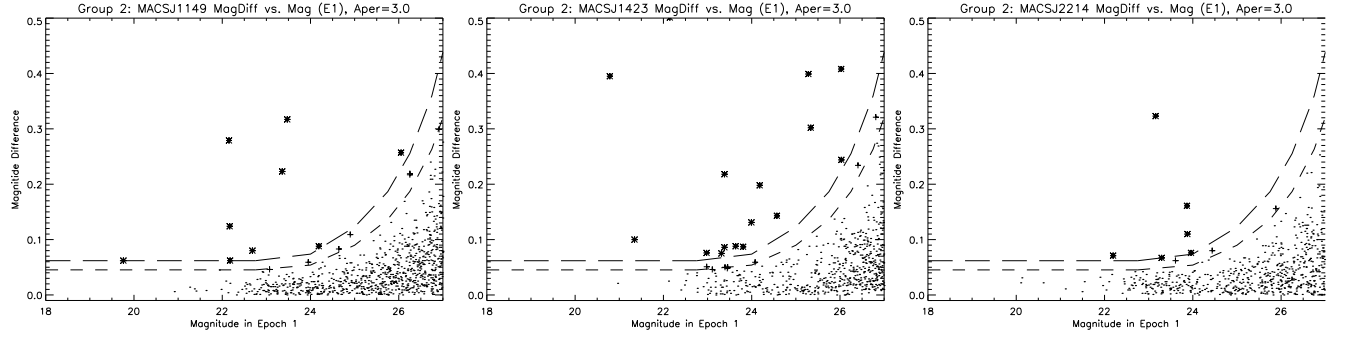


Figure 4. Plots of magnitude difference vs. magnitude in epoch 1 for all clusters in Group 2. Small dots are the data; crosses are $>3\sigma^*$ variables and asterisks are $>4\sigma^*$ variables. The short and long dashed lines illustrate the $3\sigma^*$ and $4\sigma^*$ confidence variability thresholds.

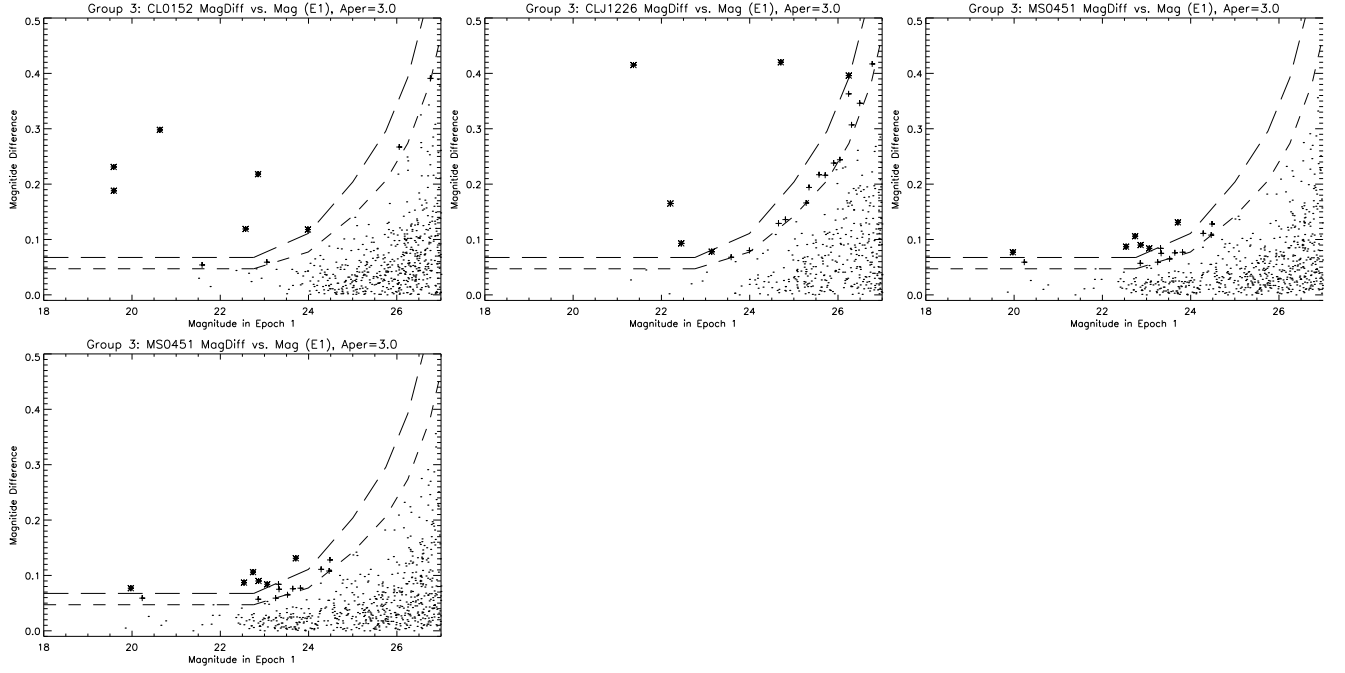


Figure 5. Plots of magnitude difference vs. magnitude in epoch 1 for all clusters in Group 3. Small dots are the data; crosses are $>3\sigma^*$ variables and asterisks are $>4\sigma^*$ variables. The short and long dashed lines illustrate the $3\sigma^*$ and $4\sigma^*$ confidence variability thresholds.

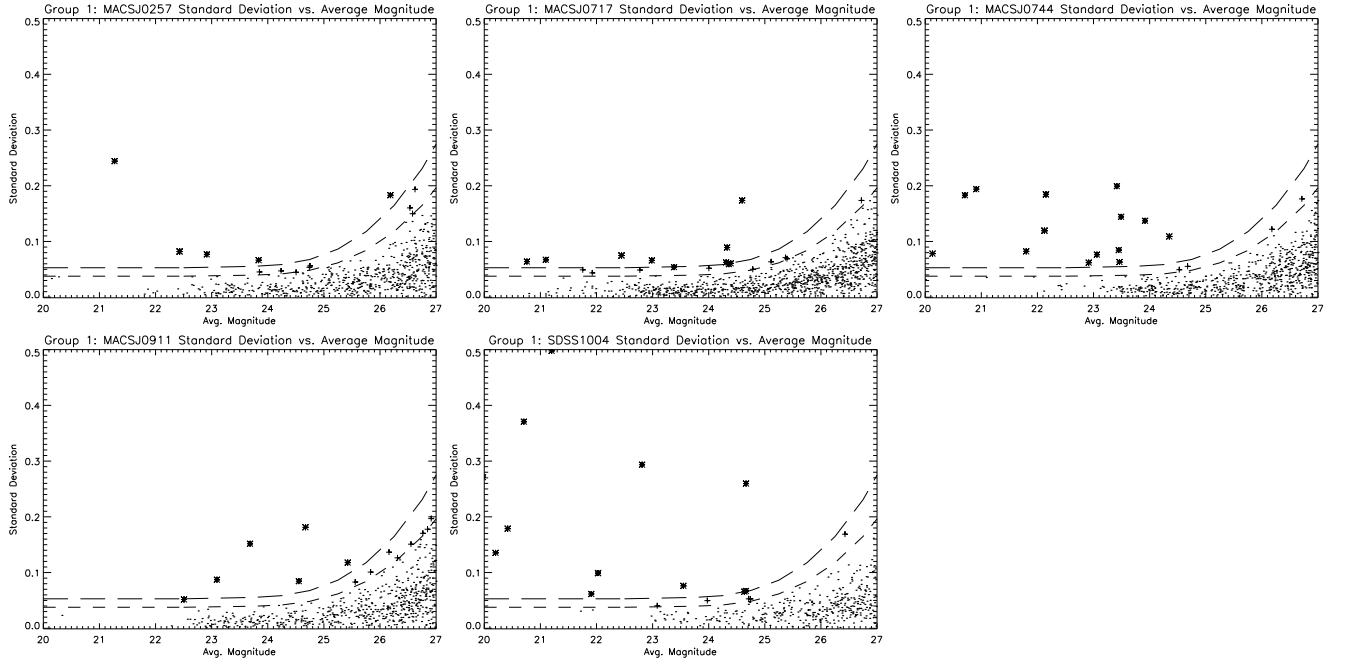


Figure 6. Plots of standard deviation vs. average magnitude for all clusters with 3 epochs of ACS data (Group 1). Small dots are the data; crosses are 3σ variables and asterisks are 4σ variables. The short and long dashed lines illustrate the 3σ and 4σ variability thresholds, respectively.

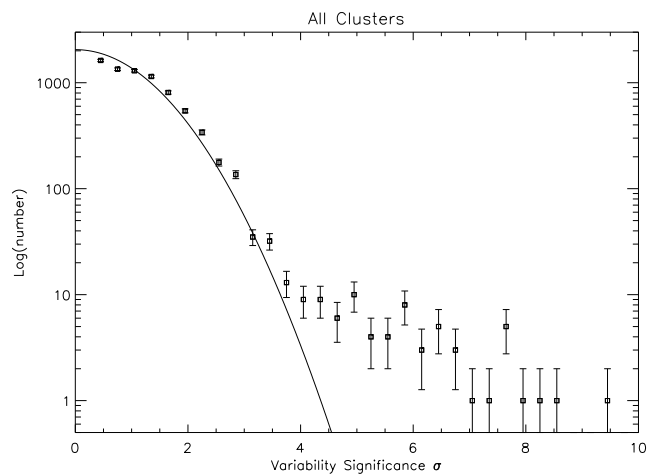


Figure 7. Distribution of σ for all galaxies in our clusters. The x-axis shows variability significance for all galaxies, normalised to remove σ^* in Groups 2 and 3. The y-axis shows the logarithm of the number of galaxies in bins of 0.3. Error bars represent the Poisson statistical errors in each bin. The solid line is a Gaussian fit to the data within 3σ .

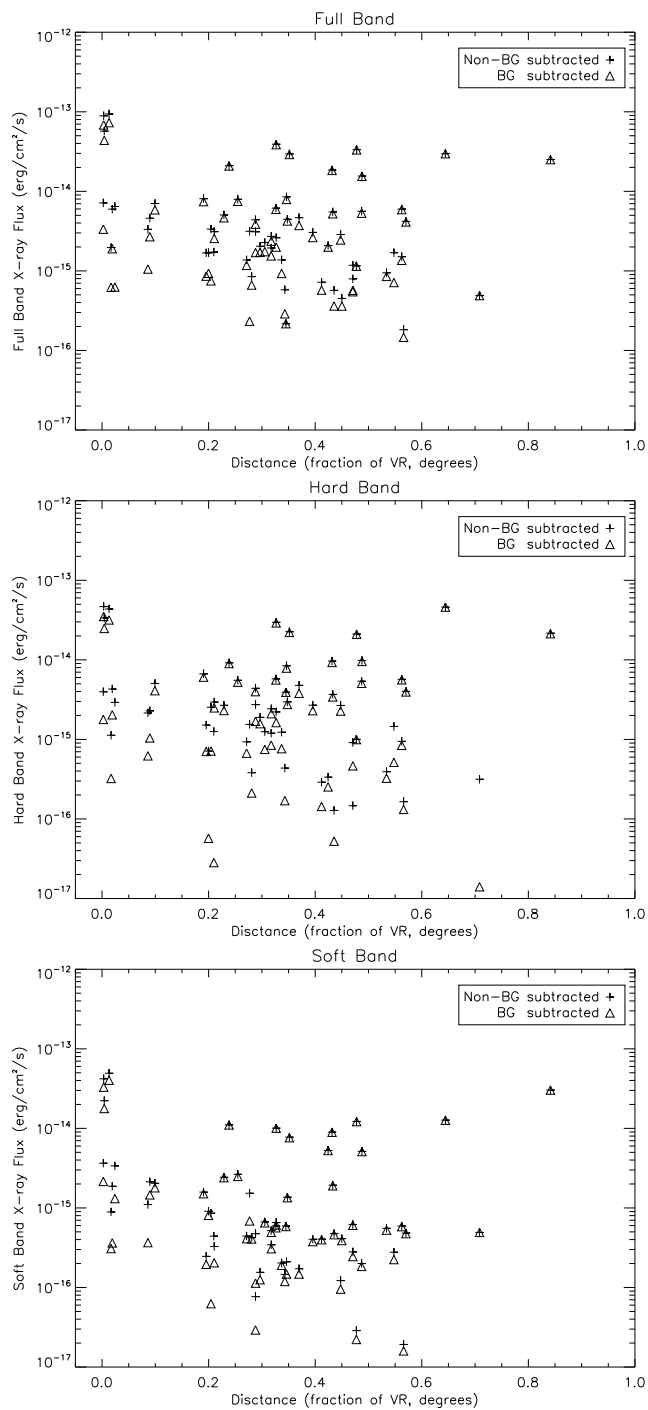


Figure 8. X-ray flux vs. distance from the center of the cluster (as a fraction of the virial radius in degrees) in the full (top), hard (middle), and soft (bottom) bands. Plus symbols are the measured fluxes, while triangles represent the background-subtracted flux (used throughout this work).

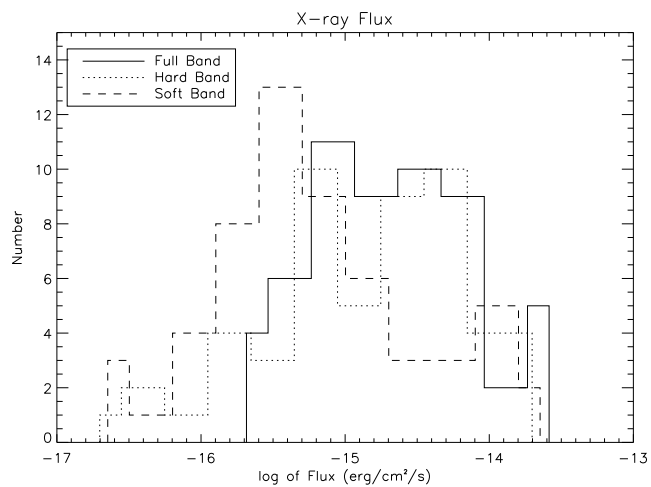


Figure 9. Histogram of the log of X-ray flux ($\text{erg/cm}^2/\text{s}$) in the full, hard, and soft bands.

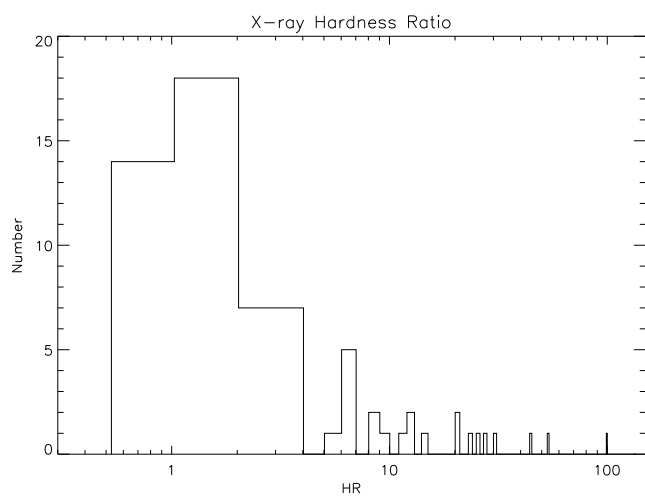


Figure 10. Histogram showing the distribution of X-ray hardness ratios for our sample of X-ray-detected AGN.

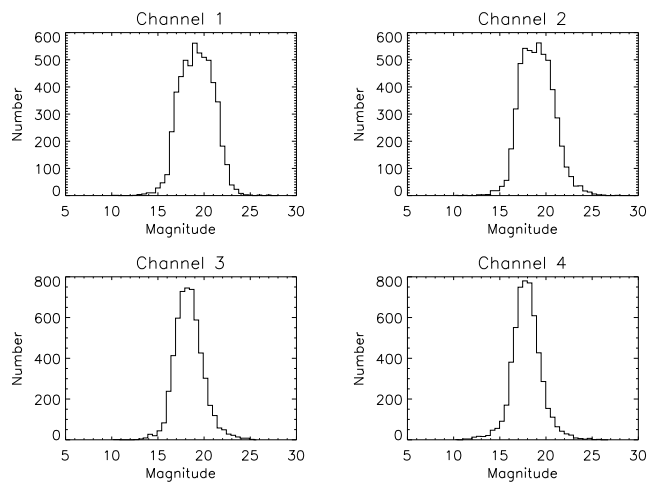


Figure 11. Histograms of IR magnitudes in each of the four Spitzer IRAC channels.

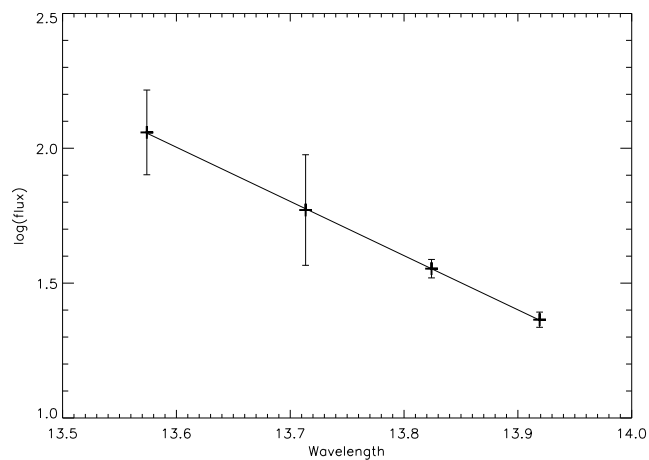


Figure 12. Example of a galaxy which shows an SED over the four IRAC channels which fit a power law model with a spectral index α between -0.5 and -2.

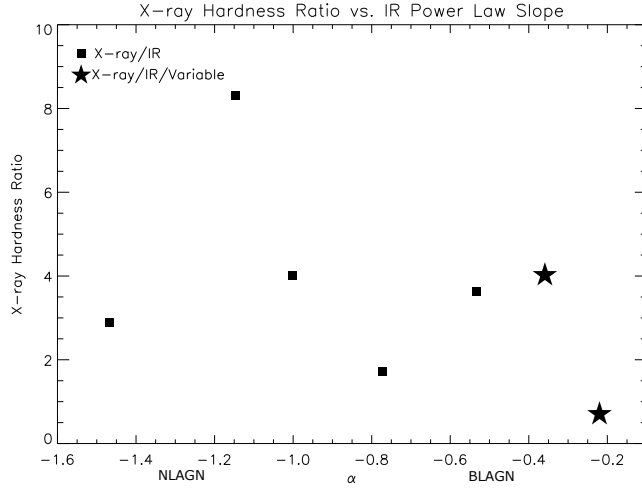


Figure 13. X-ray hardness ratio vs. IR power law slope for AGN detected in both IR and X-rays (squares). Stars denote the 2 objects which also show optical variability.

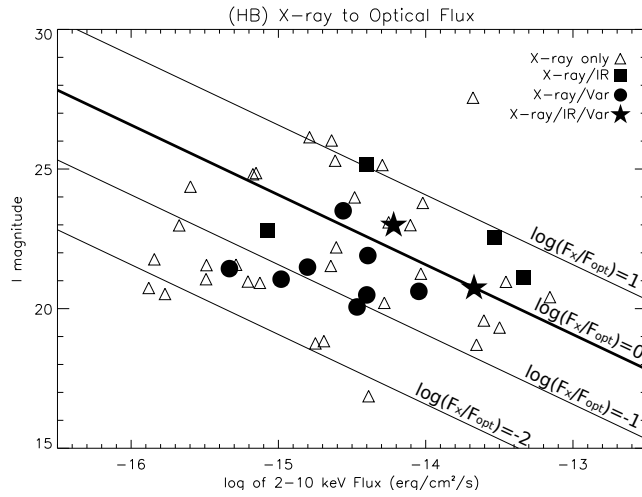


Figure 14. Optical to X-ray flux of X-ray point sources with identifiable optical counterparts; the lines indicate constant flux ratios of $\log(F_x/F_{opt}) = 1, 0, -1$, and -2 . Objects toward the top of this plot are more optically obscured, and objects toward the bottom are optically bright and X-ray weak.

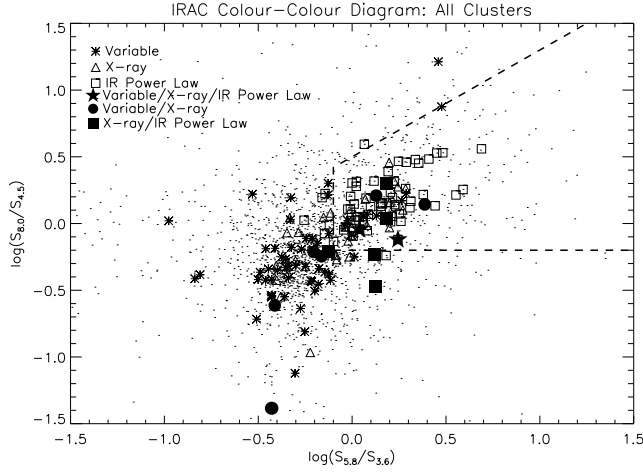


Figure 15. IRAC colour-colour plot for galaxies in all 7 clusters with Spitzer observations. The region within the dashed line is that used to select AGNs via the criteria of Lacy et al. (2007). Small points are galaxies with IR emission in all four IRAC channels, and different symbols denote the AGN detected via different techniques (see legend).

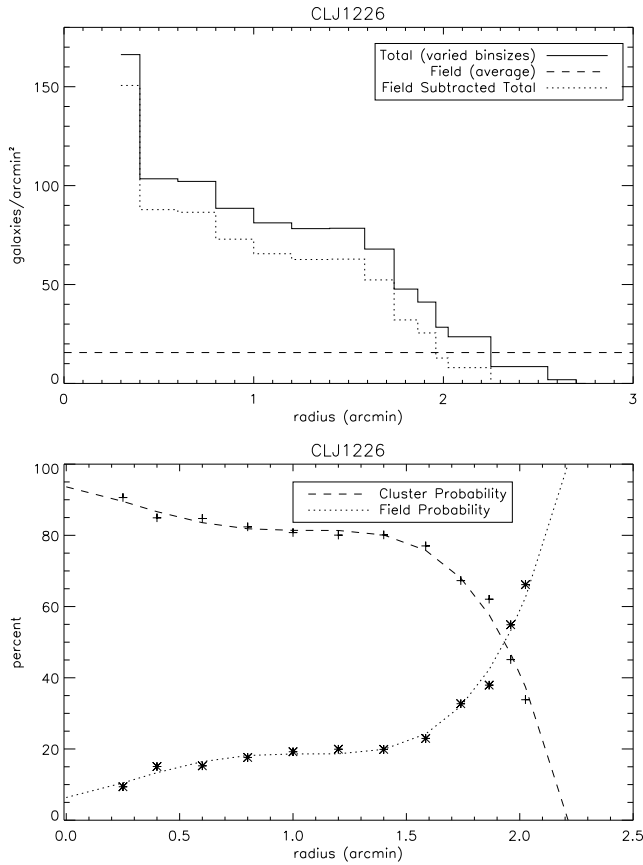


Figure 16. *Top Panel:* Radial plot of CLJ1226 showing galaxies/arcmin² vs. radial distance from the center in arcminutes. The solid histogram is the total number of objects in each radial bin and the dotted histogram is the field-subtracted radial profile of the cluster. The average number of galaxies/arcmin² is indicated with a horizontal dashed line. *Bottom Panel:* Radial plot of CLJ1226 showing the probability that a galaxy at this radius resides in the cluster (plus symbols) and the field (asterisks) as a function of distance from the center in arcminutes. The dashed and dotted lines are polynomial fits to the cluster and field probabilities.

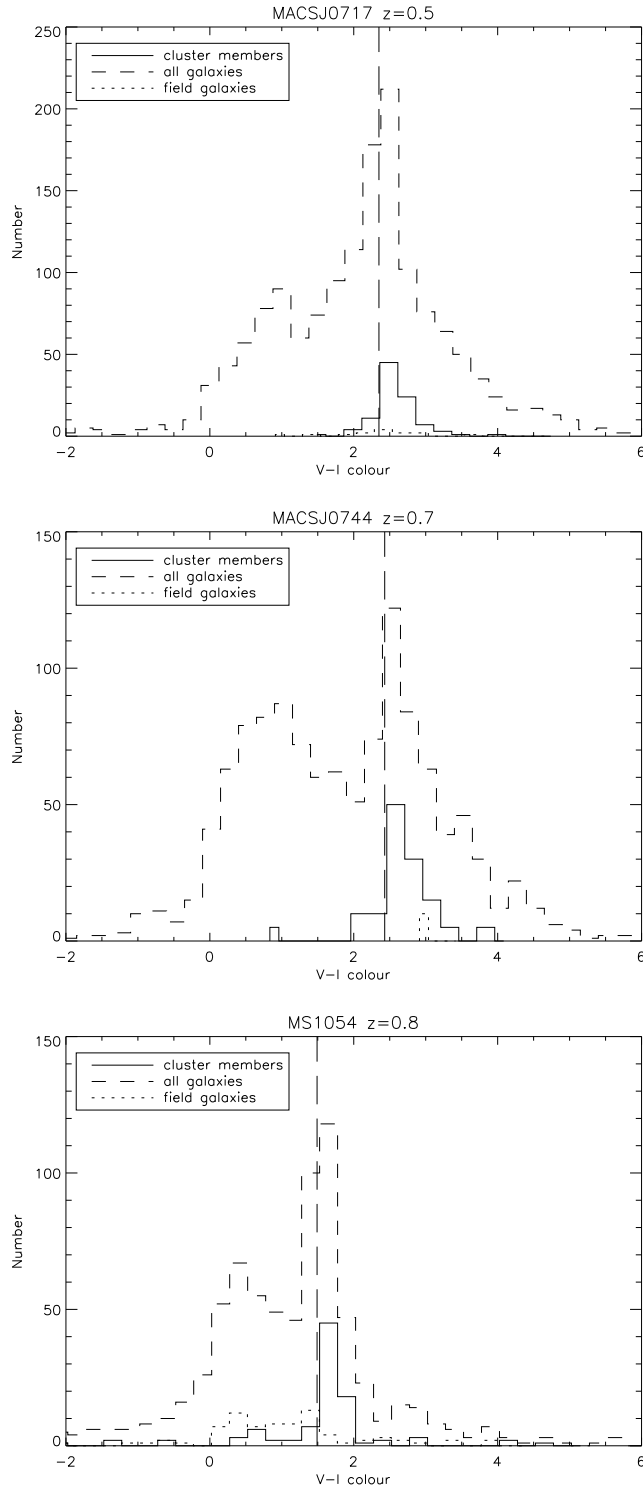


Figure 17. $V-I$ colour distributions of galaxies in MACSJ0717 (top left), MACSJ0744 (top right), and MS1054 (bottom left). The solid histogram shows the spectroscopically-confirmed cluster members and the dotted histogram shows spectroscopically-confirmed non-cluster members. The solid and dotted histograms have been scaled by a factor of 5–10 for visualisation purposes. The vertical dashed line indicates the $V-I$ colour limit for galaxies in the cluster. Galaxies redder than this limit have a greater probability of residing in the cluster.

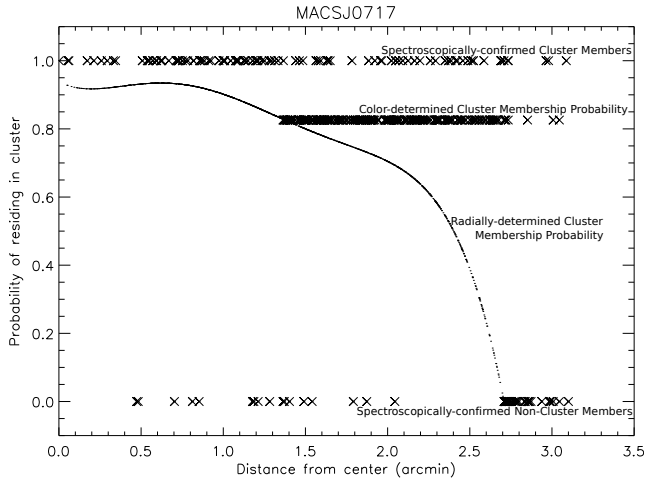


Figure 18. Radial profile of the cluster MACSJ0717, showing cluster membership probability vs. distance from the center of the cluster with cluster membership probability categories indicated.

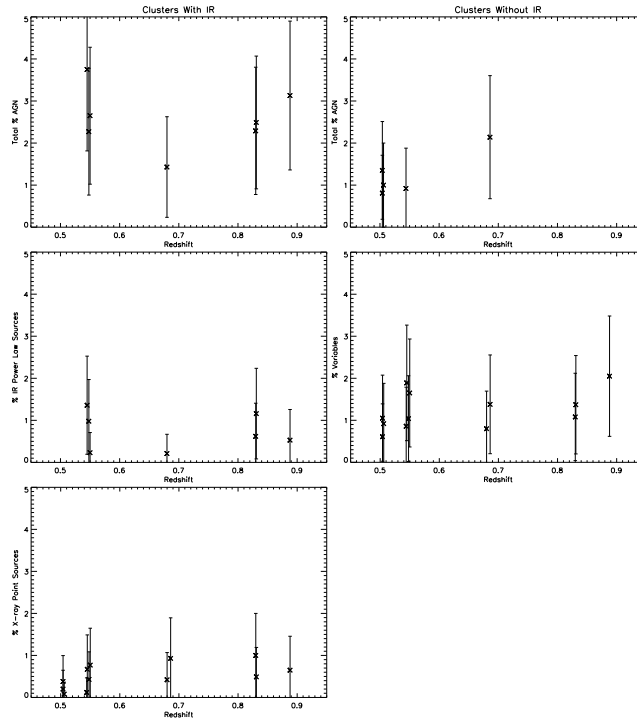


Figure 19. AGN % as a function of cluster redshift. The top two panels show the total percentage of AGN detected; the left panel shows clusters with IR observations and the right panel shows those without. The last two rows show the percentage of IR power law sources, optical variables, and X-ray point sources in each cluster.

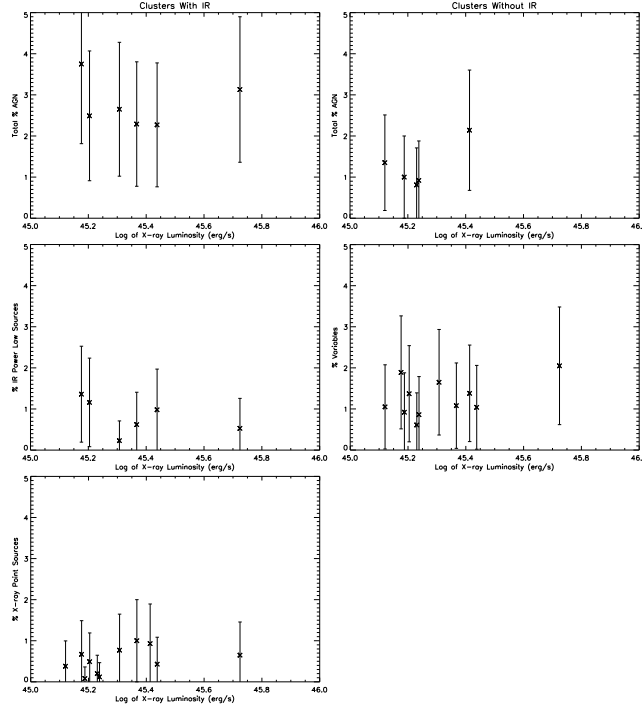


Figure 20. AGN % as a function of cluster X-ray Luminosity. The top two panels show the total percentage of AGN detected; the left panel shows clusters with IR observations and the right panel shows those without. The last two rows show the percentage of IR power law sources, optical variables, and X-ray point sources in each cluster.

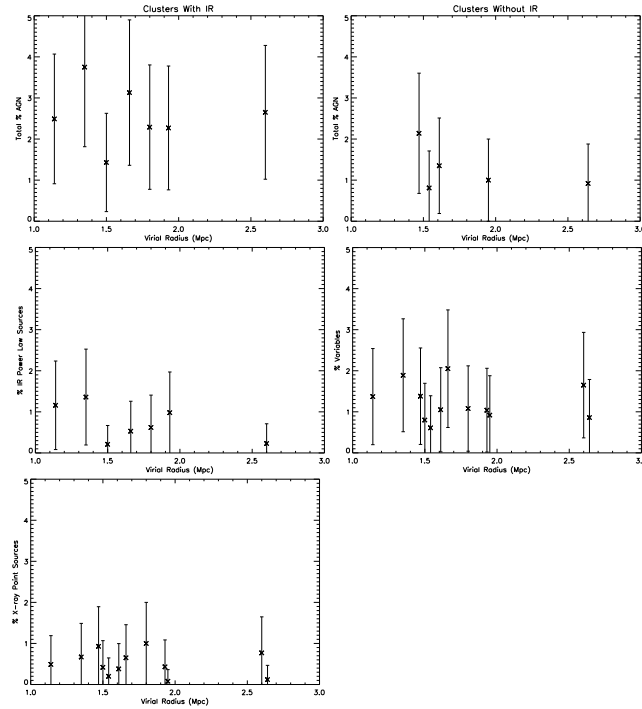


Figure 21. Percentage of AGN detected as a function of cluster virial radius (Mpc). The top two panels show the total percentage of AGN detected; the left panel shows clusters with IR observations and the right panel shows those without. The last two rows show the percentage of IR power law sources, optical variables, and X-ray point sources in each cluster.

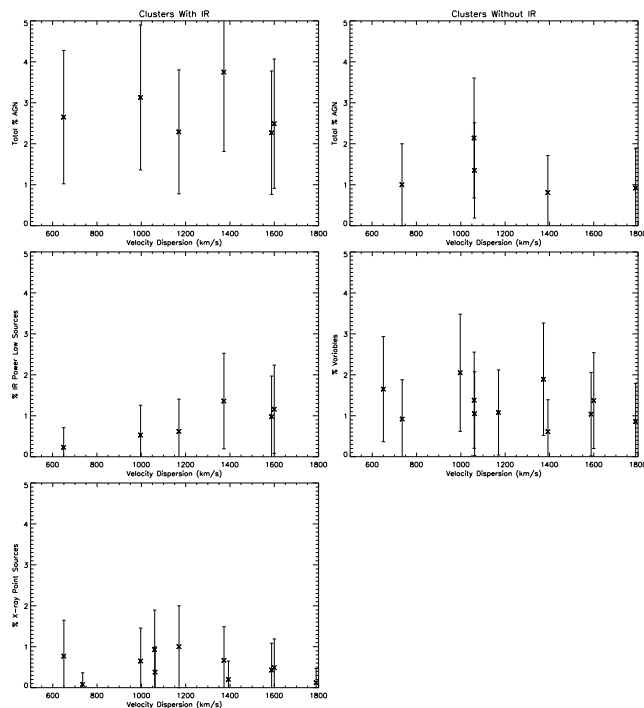


Figure 22. Percentage of AGN detected as a function of cluster velocity dispersion (km/s). The top two panels show the total percentage of AGN detected; the left panel shows clusters with IR observations and the right panel shows those without. The last two rows show the percentage of IR power law sources, optical variables, and X-ray point sources in each cluster.

Table 1. Cluster Observations

Cluster	Redshift	RA	Dec	#ACS Epochs	Obs. w/Spitzer
<i>CL</i> 0152 – 1357	0.831	01:52:43.00	-13:57:20.00	2	Y
<i>CL</i> J1226.9 + 3332	0.888	12:26:58.21	33:32:49.4	2	Y
<i>MACSJ</i> 0257 – 2325	0.506	02:57:08.83	-23:26:03.3	3	-
<i>MACSJ</i> 0717 + 3745	0.548	07:17:32.93	37:45:05.4	3	Y
<i>MACSJ</i> 0744 + 3297	0.686	07:44:52.58	39:27:26.7	3	-
<i>MACSJ</i> 0911 + 1746	0.505	09:11:11.18	17:46:34.8	3	-
<i>MACSJ</i> 1149 + 2223	0.544	11:49:35.51	22:24:04.2	2	-
<i>MACSJ</i> 1423 + 2404	0.545	14:23:48.60	24:04:49.1	2	Y
<i>MACSJ</i> 2214 – 1359	0.504	22:14:57.34	-14:00:12.2	2	-
<i>MS</i> 0451.6 – 0305	0.550	04:54:10.48	-03:01:38.5	2	Y
<i>MS</i> 1054.4 – 0321	0.830	10:57:00.20	-03:37:27.0	2	Y
<i>SDSS</i> 1004 + 41	0.680	10:04:34.72	41:12:44.98	3	Y

Table 2. Galaxy Cluster Properties

Cluster	$L_X (10^{44} \text{ erg/s})$	$M_{200} (10^{15} M_\odot)$	r_v (Mpc)	σ (km/s)
<i>CL</i> 0152 – 1357	16	0.45	1.14	1600
<i>CL</i> J1226.9 + 3332	53	1.4	1.66	997
<i>MACSJ</i> 0257.6 – 2209	15.4	1.41^1	1.95 ± 0.42	735
<i>MACSJ</i> 0717.5 + 3745	27.4	2.75^1	1.93 ± 0.28	1588
<i>MACSJ</i> 0744.8 + 3927	25.9	0.87^1	1.47 ± 0.18	1060
<i>MACSJ</i> 0911.2 + 1746	13.2	0.84^1	1.61 ± 0.50	1062
<i>MACSJ</i> 1149.5 + 2223	17.3	1.13^1	2.64 ± 0.14	1789
<i>MACSJ</i> 1423.8 + 2404	15.0	0.78^1	1.35 ± 0.19	1373
<i>MACSJ</i> 2214.9 – 1359	17.0	1.22^1	1.54 ± 0.16	1393
<i>MS</i> 0451.6 – 0305	20.3	1.4	2.6	650
<i>MS</i> 1054.4 – 0321	23.3	1.1	1.8	1170
<i>SDSS</i> 1004 + 41	-	0.42	1.35	-

¹ The value listed for M_{200} corresponds to $M_{X,200}$ derived from X-ray gas as measured by Barrett (2006)**Table 3.** ACS Observations

Cluster	#ACS Epochs	Filter(s)	Total I-band exp. time (s)
<i>CL</i> 0152 – 1357	2	F775W,F625W	4252
<i>CL</i> J1226.9 + 3332	2	F814W	4296
<i>MACSJ</i> 0257 – 2325	3	F814W,F555W	8858
<i>MACSJ</i> 0717 + 3745	3	F814W,F555W	8893
<i>MACSJ</i> 0744 + 3297	3	F814W,F555W	8893
<i>MACSJ</i> 0911 + 1746	3	F814W,F555W	8825
<i>MACSJ</i> 1149 + 2223	2	F814W,F555W	6774
<i>MACSJ</i> 1423 + 2404	2	F814W,F555W	6774
<i>MACSJ</i> 2214 – 1359	2	F814W,F555W	6640
<i>MS</i> 0451.6 – 0305	2	F814W,F555W	4198
<i>MS</i> 1054.4 – 0321	2	F775W,F606W	4232
<i>SDSS</i> 1004 + 41	3	F814W,F555W	9492

Table 4: Optical Variables: 2 Epochs

RA	Dec	Magnitude in Epoch 1	Magnitude Difference $\Delta mag_{E1} - mag_{E2}$	$\sigma\sigma^*$
Group 2				
MACSJ1149				
177.3912546	22.3741796	19.761	0.062	4.11
177.3727730	22.4131815	22.169	0.124	8.22
177.3853783	22.4158100	22.178	0.062	4.11
177.4129531	22.3912347	22.684	0.080	5.30
177.4037943	22.4045812	23.072	0.046	3.05
177.3759224	22.4014957	23.360	0.223	14.78
177.3686799	22.4041751	23.949	0.059	3.36
177.3954691	22.4100949	24.188	0.088	4.46
177.4070381	22.4083481	24.642	0.083	3.34
177.3952017	22.3798855	24.900	0.109	3.84
177.3773332	22.4018102	26.251	0.217	3.48
177.3717684	22.3879044	26.913	0.299	3.03
MACSJ1423				
215.9566994	24.0908133	20.786	0.395	26.18
215.9659128	24.0928442	21.346	0.100	6.63
215.9435626	24.1103714	22.146	0.501	33.20
215.9207094	24.0858763	22.978	0.076	5.04
215.9351613	24.0715436	22.980	0.051	3.38
215.9780502	24.0930103	23.107	0.046	3.05
215.9567855	24.1067280	23.315	0.075	4.97
215.9655477	24.0868617	23.382	0.086	5.70
215.9597155	24.0619093	23.384	0.218	14.45
215.9359890	24.1057894	23.395	0.050	3.31
215.9495924	24.0612614	23.447	0.048	3.18
215.9769087	24.0913591	23.455	0.050	3.31

Continued on Next Page...

Table 4. Continued

RA	Dec	Magnitude in Epoch 1	Magnitude Difference $\Delta mag_{E1} - mag_{E2}$	$\sigma\sigma^*$
215.9463534	24.0794877	23.636	0.088	5.75
215.9201891	24.0835353	23.806	0.087	5.29
215.9440769	24.0967723	23.994	0.131	7.30
215.9504358	24.0595245	24.077	0.059	3.16
215.9542286	24.1132513	24.181	0.198	10.07
215.9889684	24.0800075	24.571	0.143	5.97
215.9398529	24.0982543	25.284	0.399	11.45
215.9509229	24.1104959	25.338	0.302	8.41
215.9319373	24.0792266	26.026	0.408	7.57
215.9480744	24.1166938	26.030	0.244	4.52
215.9587582	24.0943249	26.407	0.234	3.38
215.9408794	24.0855590	26.811	0.321	3.50
MACSJ2214				
333.7385399	-14.0104460	22.195	0.071	4.71
333.7499718	-13.9719778	23.294	0.067	4.44
333.7583932	-13.9910634	23.607	0.062	4.09
333.7527829	-13.9949067	23.868	0.161	9.53
333.7520584	-14.0260731	23.877	0.110	6.48
333.7341329	-14.0205374	23.959	0.076	4.31
333.7235526	-14.0042341	24.439	0.080	3.57
333.7239097	-13.9995567	25.881	0.156	3.17
Group 3				
CL0152				
28.1688786	-13.9455586	19.586	0.231	14.70
28.1607732	-13.9579993	19.589	0.188	11.97
28.1644026	-13.9397735	20.632	0.298	18.97
28.1822742	-13.9837218	21.589	0.054	3.44
28.1895690	-13.9761605	22.575	0.119	7.57

Continued on Next Page...

Table 4. Continued

RA	Dec	Magnitude in Epoch 1	Magnitude Difference $\Delta mag_{E1} - mag_{E2}$	$\sigma\sigma^*$
28.1803432	-13.9825781	22.857	0.218	13.88
28.1880417	-13.9476551	23.056	0.059	3.76
28.2001421	-13.9519985	23.987	0.118	4.60
28.1794506	-13.9222247	24.572	0.572	15.17
28.1900472	-13.9502173	26.056	0.267	3.28
28.1769691	-13.9588156	26.761	0.391	3.05
28.1775526	-13.9443824	26.991	0.508	3.35
CLJ1226				
186.7312842	33.5253832	21.367	0.415	26.41
186.7377092	33.5247430	22.204	0.165	10.50
186.7134309	33.5681698	22.450	0.093	5.92
186.7523004	33.5801296	23.139	0.078	4.96
186.7243970	33.5165821	23.579	0.068	3.64
186.7250854	33.5310650	23.994	0.080	3.10
186.7740200	33.5685422	24.652	0.129	3.27
186.7668703	33.5461438	24.705	0.420	10.34
186.7394608	33.5543693	24.808	0.136	3.17
186.7343484	33.5454170	25.279	0.166	3.06
186.7525110	33.5679691	25.343	0.194	3.46
186.7231011	33.5228074	25.570	0.217	3.46
186.7694897	33.5374895	25.710	0.216	3.21
186.7535286	33.5764757	25.902	0.238	3.19
186.7602496	33.5469954	26.043	0.244	3.02
186.7576560	33.5509848	26.240	0.363	4.00
186.7464187	33.5792817	26.244	0.396	4.35
186.7453473	33.5511519	26.307	0.307	3.24
186.7545107	33.5428447	26.492	0.346	3.25
186.7228116	33.5524832	26.775	0.417	3.22

Continued on Next Page...

Table 4. Continued

RA	Dec	Magnitude in Epoch 1	Magnitude Difference $\Delta mag_{E1} - mag_{E2}$	$\sigma\sigma^*$
MS0451				
73.5310816	-3.0242817	19.973	0.077	4.90
73.5470245	-3.0189210	20.231	0.059	3.76
73.5602406	-3.0217034	22.537	0.087	5.54
73.5400210	-3.0554742	22.741	0.106	6.75
73.5469272	-3.0081061	22.858	0.057	3.63
73.5429796	-3.0128456	22.866	0.090	5.73
73.5219066	-3.0094232	23.252	0.059	3.93
73.5352979	-3.0218088	23.317	0.084	5.41
73.5418986	-3.0116541	23.330	0.075	4.79
73.5359322	-3.0150495	23.521	0.065	3.64
73.5515820	-3.0379746	23.641	0.076	3.88
73.5400868	-3.0097906	23.710	0.131	6.33
73.5583410	-3.0463730	23.815	0.077	3.43
73.5440042	-3.0142335	24.283	0.111	3.52
73.5396628	-3.0067494	24.465	0.108	3.05
73.5386585	-3.0070093	24.483	0.128	3.58
MS1054				
164.2418732	-3.6166539	20.754	0.054	3.44
164.2872055	-3.6180837	21.034	0.061	3.88
164.2709896	-3.6276280	21.584	0.066	4.20
164.2512256	-3.6036362	21.707	0.110	7.00
164.2512507	-3.6259795	22.044	0.052	3.31
164.2641578	-3.6201692	22.703	0.048	3.06
164.2268129	-3.6389238	22.732	0.096	6.11
164.2510498	-3.6023293	23.543	0.081	4.46
164.2618582	-3.5985359	23.833	0.077	3.38
164.2892100	-3.6185126	25.899	0.224	3.01

Continued on Next Page...

Table 4. Continued

RA	Dec	Magnitude in Epoch 1	Magnitude Difference $\Delta mag_{E1} - mag_{E2}$	$\sigma\sigma^*$
164.2578790	-3.6210164	26.132	0.287	3.37

Table 5: Optical Variables: 3 Epochs

RA	Dec	Average Magnitude	Standard Deviation	σ
MACSJ0257				
44.3055608	-23.4389531	21.270	0.244	19.39
44.2958934	-23.4440126	22.429	0.082	6.51
44.3086292	-23.4349091	22.914	0.077	5.88
44.2831760	-23.4615253	23.837	0.066	5.01
44.2698898	-23.4558108	23.851	0.045	3.42
44.2980084	-23.4009620	24.237	0.047	3.40
44.2826153	-23.4625286	24.504	0.045	3.02
44.3141248	-23.4306697	24.741	0.054	3.34
44.2738603	-23.4679200	24.752	0.056	3.48
44.2790992	-23.4070071	26.185	0.183	4.88
44.2930862	-23.4263251	26.534	0.160	3.37
44.3088571	-23.4484059	26.580	0.150	3.06
44.2747144	-23.4545009	26.625	0.194	3.83
MACSJ0717				
109.3844234	37.7426021	20.760	0.064	5.08
109.3918103	37.7457797	21.097	0.067	5.33
109.3833442	37.7651780	21.755	0.049	3.90
109.4096445	37.7411693	21.925	0.044	3.47
109.4049328	37.7713700	22.446	0.075	5.94
109.4093465	37.7805529	22.773	0.049	3.76
109.3975852	37.7262858	22.986	0.066	5.04
109.3662483	37.7257533	23.382	0.054	4.11
109.3769526	37.7696201	24.002	0.052	3.87
109.3965779	37.7614963	24.311	0.063	4.43
109.3720647	37.7299507	24.329	0.089	6.29
109.4055485	37.7603481	24.360	0.059	4.15

Continued on Next Page...

Table 5. Continued

RA	Dec	Average Magnitude	Standard Deviation	σ
109.3943799	37.7543835	24.393	0.061	4.22
109.4156913	37.7746773	24.597	0.174	11.37
109.4102631	37.7818927	24.786	0.050	3.06
109.4092287	37.7723866	25.111	0.064	3.33
109.4122641	37.7441675	25.368	0.071	3.23
109.4027451	37.7600369	25.395	0.069	3.09
109.3911791	37.7572230	26.721	0.174	3.22
MACSJ0744				
116.2370239	39.4521806	20.131	0.078	6.21
116.1913481	39.4654650	20.709	0.183	14.54
116.1978413	39.4703712	20.909	0.194	15.40
116.2428748	39.4462864	21.801	0.082	6.53
116.2355629	39.4630655	22.126	0.119	10.45
116.2517900	39.4484170	22.152	0.185	15.99
116.2472209	39.4448490	22.914	0.062	4.75
116.2170532	39.4614499	23.060	0.076	5.83
116.2130861	39.4560138	23.416	0.199	15.19
116.2478060	39.4489390	23.450	0.085	6.44
116.2620875	39.4579688	23.463	0.063	4.81
116.2365784	39.4579739	23.491	0.144	10.99
116.2421946	39.4566573	23.918	0.137	10.28
116.2160874	39.4648555	24.351	0.109	7.65
116.2089954	39.4516673	24.528	0.049	3.30
116.1913103	39.4680458	24.676	0.055	3.53
116.2199359	39.4618170	26.178	0.122	3.27
116.1984564	39.4732781	26.713	0.176	3.29
MACSJ0911				
137.7940737	17.7815756	22.507	0.052	4.10

Continued on Next Page...

Table 5. Continued

RA	Dec	Average Magnitude	Standard Deviation	σ
137.7975928	17.7737486	23.094	0.087	6.64
137.8182848	17.7942812	23.684	0.152	11.52
137.7764971	17.7593495	24.554	0.085	7.65
137.7982000	17.7991657	24.672	0.181	5.62
137.7976206	17.7646814	25.424	0.118	11.56
137.7970113	17.7770408	25.558	0.083	3.41
137.7946857	17.7580568	25.832	0.101	5.18
137.7828215	17.7554113	26.161	0.137	3.36
137.8110781	17.7915322	26.312	0.126	3.71
137.7817890	17.7674166	26.552	0.151	3.09
137.8038016	17.7992679	26.764	0.170	3.22
137.7992320	17.7912202	26.848	0.178	3.14
137.8039463	17.7922739	26.912	0.197	3.03
SDSS1004				
151.1303675	41.2041108	20.201	0.135	10.75
151.1301931	41.2094474	21.906	0.062	4.89
151.1348809	41.2229035	22.028	0.099	7.87
151.1549556	41.2090281	22.813	0.293	22.56
151.1522328	41.2099695	23.083	0.040	3.08
151.1491160	41.2287387	23.548	0.076	5.80
151.1321475	41.1969242	23.975	0.050	3.71
151.1393206	41.2018582	24.663	0.067	3.32
151.1276793	41.2231389	24.665	0.260	3.28
151.1361980	41.2013971	24.713	0.053	7.65
151.1410923	41.2026046	24.743	0.053	4.28

Table 6. X-ray Observations

Cluster	Obs IDs	Effective Exp. Time (ks)
<i>CLJ</i> 0152 – 1357	913	34.79
<i>CLJ</i> 1226.9 + 3332	3180, 5014	56.6
<i>MACSJ</i> 0257 – 2325	1654, 3518	36.27
<i>MACSJ</i> 0717 + 3745	1655, 4200	74.98
<i>MACSJ</i> 0744 + 3297	3197, 3585, 6111	86.49
<i>MACSJ</i> 0911 + 1746	3587, 5012	39.11
<i>MACSJ</i> 1149 + 2223	1656, 3589	36.04
<i>MACSJ</i> 1423 + 2404	1657, 4195	131.65
<i>MACSJ</i> 2214 – 1359	3259, 5011	35.07
<i>MS</i> 0451.6 – 0305	529, 902	84.59
<i>MS</i> 1054.4 – 0321	512	55.81
<i>SDSS</i> 1004 + 41	5794	73.89

Table 7: X-ray Point Sources

RA	Dec	Source	Full Band Flux	Hard Band Flux	Soft Band Flux	Full Band	Hard Band	Soft Band	Hardness
		Significance	(10^{-14} erg/cm ² /s)	(10^{-14} erg/cm ² /s)	(10^{-14} erg/cm ² /s)	Luminosity	Luminosity	Luminosity	Ratio
						(10^{42} erg/s)	(10^{42} erg/s)	(10^{42} erg/s)	
CL0152									
28.1822599	-13.9837439	119.6	2.50	2.13	3.03	83.13	70.71	100.45	0.704
28.1658054	-13.9614279	99.7	2.97	4.59	1.27	98.65	152.55	42.01	3.631
28.2054645	-13.9494400	2.9	0.02	0.39	0.06	0.72	13.00	1.94	6.713
28.1794661	-13.9222264	3.4	0.05	0.001	0.05	1.62	0.05	1.63	0.029
CLJ1226									
186.7745191	33.5371130	39.1	1.54	0.96	0.51	60.44	37.40	19.99	1.871
186.7306779	33.5619212	4.5	0.07	0.02	0.04	2.59	0.83	1.59	0.522
186.7648292	33.5486789	6.8	0.15	0.08	0.05	6.04	3.32	1.93	1.716
186.7713414	33.5708274	4.3	0.60	0.56		23.07	21.95		
186.7470370	33.5726419	3.7	0.20	0.03	0.52	7.79	1.0	20.63	0.048
186.7426687	33.5473250	6.0	0.06	0.03	0.03	2.43	1.26	1.21	1.047
MACSJ0257									
44.2864042	-23.4347195	22.3	0.33	0.18	0.22	3.28	1.75	2.11	
MACSJ0717									
109.3965517	37.7614859	15.2	0.74	0.61	0.15	8.84	7.21	1.79	4.023
109.3723440	37.7299276	3.4	0.17	0.16	0.01	2.04	1.88	0.15	12.598
109.3733968	37.7355905	23.8	0.75	0.52	0.25	8.91	6.23	2.96	2.107
109.4049424	37.7394916	14.0	0.59	0.41	0.18	6.97	4.88	2.13	2.288
109.4095429	37.7710936	8.0	0.20	0.16	0.06	2.37	1.94	0.73	2.669
109.4094130	37.7804483	16.8	0.52	0.34	0.19	6.22	4.07	2.26	1.802
109.3827366	37.7585013	7.8		0.003			0.03		
109.3747064	37.7599473	5.5	0.02		0.07	0.28		0.82	
109.3804777	37.7559334	5.3	0.07	0.07	0.006	0.89	0.85	0.07	11.429
MACSJ0744									

Continued on Next Page...

Table 7. Continued

RA	Dec	Source	Full Band Flux	Hard Band Flux	Soft Band Flux	Full Band	Hard Band	Soft Band	Hardness
		Significance	(10^{-14} erg/cm ² /s)	(10^{-14} erg/cm ² /s)	(10^{-14} erg/cm ² /s)	Luminosity	Luminosity	Luminosity	Ratio
						(10^{42} erg/s)	(10^{42} erg/s)	(10^{42} erg/s)	
116.2129909	39.4559733	18.8	0.27	0.10	0.15	5.55	2.15	3.01	0.716
116.2355557	39.4629842	72.8	2.08	0.90	1.10	42.98	18.55	22.76	0.815
116.2338550	39.4414446	8.9	0.59	0.56	0.06	12.27	11.52	1.16	9.928
116.2261739	39.4463955	8.2	0.09	0.006	0.08	1.93	0.12	1.67	0.071
116.2197114	39.4570427	113.3	4.38	2.48	1.78	90.46	51.28	36.66	1.399
116.2255481	39.4590797	10.2	0.11	0.06	0.04	2.18	1.28	0.76	1.694
116.1825316	39.4681158	4.4	0.09	0.03	0.05	1.76	0.67	1.08	0.618
116.2235061	39.4722130	5.6	0.12	0.07	0.04	2.42	1.39	0.85	1.634
116.2386419	39.4782976	3.0	0.04		0.04	0.75		0.80	
116.2061638	39.4795673	3.0	0.04	0.005	0.05	0.75	0.11	0.95	0.114
116.2101346	39.4828672	3.4	0.05		0.06	1.13		1.25	
116.2191062	39.4555426	15.5	0.06		0.13	1.29		2.71	
MACSJ0911									
137.7735912	17.7549356	3.3	0.06	0.01	0.04	0.56	0.14	0.39	0.361
137.7764594	17.7593429	5.9	0.42	0.28	0.13	4.12	2.67	1.31	2.048
137.7828408	17.7573540	5.0	0.17	0.07	0.07	1.70	0.73	0.63	1.151
137.8133826	17.7664873	6.9	0.47	0.23	0.24	4.52	2.24	2.33	0.962
137.7819338	17.8020018	41.2	1.83	0.93	0.89	17.80	9.01	8.68	1.037
MACSJ1149									
177.3912459	22.3741690	38.0	2.90	2.21	0.76	33.97	25.87	8.92	2.901
177.4317201	22.4084066	3.1	0.24	0.23	0.01	2.86	2.65	0.11	23.785
MACSJ1423									
215.9495972	24.0612389	7.7	0.39	0.40	0.003	4.54	4.68	0.03	136.351
215.9374553	24.0612913	12.3	0.79	0.79	0.01	9.29	9.25	0.17	53.388
215.9395923	24.0620335	6.1	0.24	0.21	0.03	2.77	2.47	0.36	6.847
215.9499484	24.0778332	468.7	6.83	3.51	3.29	80.19	41.19	38.69	1.065

Continued on Next Page...

Table 7. Continued

RA	Dec	Source	Full Band Flux	Hard Band Flux	Soft Band Flux	Full Band	Hard Band	Soft Band	Hardness
		Significance	(10^{-14} erg/cm ² /s)	(10^{-14} erg/cm ² /s)	(10^{-14} erg/cm ² /s)	Luminosity	Luminosity	Luminosity	Ratio
						(10^{42} erg/s)	(10^{42} erg/s)	(10^{42} erg/s)	
215.9244969	24.0783396	9.9	0.26	0.23	0.04	3.09	2.70	0.44	6.087
215.9496258	24.0783947	453.2	7.31	3.17	4.03	85.87	37.27	47.35	0.787
215.9206991	24.0858974	5.1	0.06	0.05	0.02	0.67	0.55	0.29	1.900
215.9604737	24.1098496	4.5	0.01	0.01	0.002	0.17	0.15	0.02	8.260
215.9706757	24.1040500	3.9	0.07	0.05	0.02	0.84	0.61	0.26	2.298
215.9713530	24.0824452	3.0	0.03	0.02	0.01	0.34	0.20	0.14	1.427
MACSJ2214									
333.7058150	-13.9927152	57.8	3.32	2.09	1.22	32.25	20.36	11.81	1.724
333.7037453	-13.9987859	4.6	0.53	0.51	0.02	5.16	4.93	0.18	27.601
333.7527550	-13.9661911	3.2	0.14	0.08	0.06	1.32	0.82	0.57	1.448
333.7385399	-14.0034419	7.6	0.19	0.20	0.04	1.84	2.0	0.35	5.610
MS0451									
73.5532701	-3.0131560	20.0	0.54	0.27	0.26	6.46	3.24	3.14	1.033
73.5666479	-3.0426321	6.3	0.66	0.71	0.03	7.87	8.58	0.41	20.923
73.5525164	-3.0210133	5.7	0.61	0.59	0.03	7.36	7.06	0.34	20.825
73.5441260	-2.9945854	2.9	0.14	0.11	0.03	1.65	1.36	0.34	4.013
73.5451998	-3.0236520	4.2	0.05		0.06	0.62		0.73	
73.5469876	-3.0183918	14.8	0.17	0.15	0.04	2.06	1.76	0.47	3.717
73.5477995	-3.0159639	10.6	0.48	0.45	0.07	5.79	5.43	0.90	6.053
MS1054									
164.2608788	-3.6620178	15.0	0.41	0.39	0.05	13.63	13.07	1.57	8.307
164.2446619	-3.6473165	147.8	3.86	2.91	1.00	127.76	96.43	33.25	2.900
164.2728766	-3.6470993	3.8	0.11	0.10	0.002	3.79	3.29	0.07	44.849
164.2700806	-3.6390165	7.0	0.37	0.38	0.01	12.32	12.57	0.49	25.758
164.2510953	-3.6135971	4.3	0.09	0.07	0.02	2.84	2.34	0.65	3.609
164.2343522	-3.6099210	5.8	0.09	0.08	0.02	3.07	2.53	0.63	4.022

Continued on Next Page...

Table 7. Continued

RA	Dec	Source	Full Band Flux	Hard Band Flux	Soft Band Flux	Full Band	Hard Band	Soft Band	Hardness
		Significance	(10^{-14} erg/cm ² /s)	(10^{-14} erg/cm ² /s)	(10^{-14} erg/cm ² /s)	Luminosity	Luminosity	Luminosity	Ratio
						(10^{42} erg/s)	(10^{42} erg/s)	(10^{42} erg/s)	
164.2305684	-3.6294611	4.3	0.17	0.17	0.01	5.63	5.58	0.38	14.882
164.2359270	-3.6226173	4.8	0.26	0.25	0.02	8.47	8.24	0.68	12.167
SDSS1004									
151.1429380	41.2057254	258.5	9.07	6.97	2.02	183.31	140.84	40.81	3.451
151.1549890	41.2089868	52.9	0.90	0.40	0.52	18.13	8.18	10.46	0.782
151.1404309	41.2187712	10.8	0.39	0.33	0.05	7.87	6.65	1.07	6.227
151.1276141	41.2350108	10.9	0.07		0.11	1.35		2.28	
151.1267442	41.2374555	7.1	0.25	0.25	0.002	5.11	4.99	0.05	99.886
151.1614315	41.2139738	4.4	0.27	0.24	0.008	5.43	4.91	0.16	30.132

Table 8. Rest-Frame X-ray Fitting Parameters

Cluster	Redshift	$n_H(10^{20} \text{ cm}^{-2})$	D_L (10^3 Mpc)
<i>CLJ</i> 0152 – 1357	0.831	1.58	5.2675
<i>CLJ</i> 1226.9 + 3332	0.888	1.37	5.7207
<i>MACSJ</i> 0257 – 2325	0.506	2.16	2.8636
<i>MACSJ</i> 0717 + 3745	0.548	7.11	3.1546
<i>MACSJ</i> 0744 + 3297	0.686	5.62	4.1540
<i>MACSJ</i> 0911 + 1746	0.504	3.64	2.8499
<i>MACSJ</i> 1149 + 2223	0.544	2.21	3.1266
<i>MACSJ</i> 1423 + 2404	0.545	2.28	3.1336
<i>MACSJ</i> 2214 – 1359	0.504	3.30	2.8499
<i>MS</i> 0451.6 – 0305	0.550	5.03	3.1686
<i>MS</i> 1054.4 – 0321	0.830	3.62	5.2596
<i>SDSS</i> 1004 + 41	0.680	1.11	4.1092

Table 9: IR Power Law Galaxies

RA	Dec	Channel 1 Flux (μ Jy)	Channel 2 Flux (μ Jy)	Channel 3 Flux (μ Jy)	Channel 4 Flux (μ Jy)	α
CL0152						
28.1822554	-13.9837263	84.382 ± 0.03	88.462 ± 0.03	96.722 ± 0.21	99.831 ± 0.16	-0.220 ± 0.005
28.1657731	-13.9614409	316.814 ± 0.03	341.394 ± 0.03	425.256 ± 0.21	552.300 ± 0.16	-0.534 ± 0.348
28.2023977	-13.9609316	6.262 ± 0.03	7.842 ± 0.03	12.860 ± 0.20	11.498 ± 0.16	-0.948 ± 0.524
28.2118833	-13.9445033	9.623 ± 0.03	10.218 ± 0.03	16.433 ± 0.20	13.709 ± 0.16	-0.429 ± 0.649
28.2002399	-13.9685599	4.550 ± 0.03	5.340 ± 0.03	4.764 ± 0.20	5.670 ± 0.16	-0.463 ± 0.721
28.1785907	-13.9401408	1.416 ± 0.03	1.910 ± 0.03	3.398 ± 0.21	3.143 ± 0.16	-1.241 ± 0.727
28.1902671	-13.9546800	15.310 ± 0.03	17.536 ± 0.03	16.802 ± 0.21	15.846 ± 0.16	-0.313 ± 0.899
28.1497103	-13.9553142	4.759 ± 0.03	4.949 ± 0.03	8.497 ± 0.20	5.837 ± 0.16	-0.307 ± 0.972
28.1889414	-13.9704190	3.667 ± 0.03	3.725 ± 0.03	6.175 ± 0.20	5.173 ± 0.16	-0.331 ± 1.056
CLJ1226						
186.7831346	33.5422895	7.047 ± 0.02	9.017 ± 0.04	11.268 ± 0.16	15.481 ± 0.16	-1.049 ± 0.054
186.7648601	33.5486663	13.674 ± 0.02	16.264 ± 0.04	21.723 ± 0.16	23.397 ± 0.16	-0.772 ± 0.118
186.7622048	33.5810414	3.532 ± 0.02	4.024 ± 0.04	5.789 ± 0.16	6.286 ± 0.16	-0.720 ± 0.267
186.7723818	33.5404982	9.742 ± 0.02	11.192 ± 0.04	9.535 ± 0.16	14.330 ± 0.16	-0.467 ± 0.614
186.7770329	33.5674392	2.420 ± 0.02	2.819 ± 0.04	3.957 ± 0.16	3.208 ± 0.16	-0.606 ± 0.655
186.7406772	33.5741832	8.603 ± 0.02	10.191 ± 0.04	9.839 ± 0.16	10.474 ± 0.16	-0.477 ± 0.766
186.7582612	33.5493497	4.683 ± 0.02	6.803 ± 0.04	7.283 ± 0.16	16.658 ± 0.16	-1.542 ± 0.819
186.7807553	33.5305652	11.133 ± 0.02	12.925 ± 0.04	13.438 ± 0.16	11.405 ± 0.16	-0.365 ± 1.024
MACSJ0717						
109.3928291	37.7245885	2.935 ± 0.06	2.923 ± 0.08	3.148 ± 0.32	3.255 ± 0.35	-0.071 ± 0.016
109.3629996	37.7337217	12.555 ± 0.06	12.858 ± 0.08	18.233 ± 0.33	18.016 ± 0.35	-0.366 ± 0.159
109.3558296	37.7535242	2.964 ± 0.06	3.207 ± 0.08	2.244 ± 0.33	3.146 ± 0.35	-0.087 ± 0.277
109.3840303	37.7460376	9.658 ± 0.06	11.164 ± 0.08	9.666 ± 0.33	22.502 ± 0.35	-0.730 ± 0.320
109.4163527	37.7292860	21.710 ± 0.06	27.736 ± 0.08	34.780 ± 0.33	28.593 ± 0.35	-0.768 ± 0.329
109.3965342	37.7614894	80.344 ± 0.06	95.472 ± 0.08	74.035 ± 0.33	90.152 ± 0.35	-0.359 ± 0.381
109.3934829	37.7643657	53.588 ± 0.06	52.944 ± 0.08	38.442 ± 0.33	88.598 ± 0.35	-0.138 ± 0.549
109.4106889	37.7394504	13.860 ± 0.06	12.896 ± 0.08	14.578 ± 0.32	24.543 ± 0.35	-0.191 ± 0.584
109.3793892	37.7485335	6.242 ± 0.06	6.358 ± 0.08	12.673 ± 0.33	8.346 ± 0.35	-0.430 ± 0.610
109.3908128	37.7694448	5.769 ± 0.06	4.976 ± 0.08	5.664 ± 0.33	7.951 ± 0.35	0.110 ± 0.627
109.3738374	37.7252618	1.882 ± 0.06	2.846 ± 0.08	9.206 ± 0.33	10.313 ± 0.35	-2.232 ± 0.658
109.3810264	37.7676157	1.138 ± 0.06	1.625 ± 0.08	4.445 ± 0.32	2.915 ± 0.35	-1.636 ± 0.823
109.3855832	37.7682947	5.787 ± 0.06	4.886 ± 0.08	8.234 ± 0.33	6.579 ± 0.35	0.130 ± 0.893
109.3732827	37.7723907	1.101 ± 0.06	1.459 ± 0.08	1.939 ± 0.33	1.111 ± 0.35	-0.723 ± 0.921
109.3818543	37.7683655	1.468 ± 0.06	2.047 ± 0.08	1.703 ± 0.33	8.049 ± 0.35	-1.596 ± 0.942
109.3567558	37.7543811	3.573 ± 0.06	3.656 ± 0.08	6.319 ± 0.32	10.675 ± 0.35	-0.828 ± 0.968
109.3580546	37.7657923	4.023 ± 0.06	4.209 ± 0.08	9.123 ± 0.33	11.918 ± 0.35	-0.948 ± 1.073
109.4086503	37.7712752	3.446 ± 0.06	4.218 ± 0.08	12.289 ± 0.33	6.895 ± 0.35	-1.183 ± 1.086
MACSJ1423						

Continued on Next Page. . .

Table 9. Continued

RA	Dec	Channel 1 Flux (μ Jy)	Channel 2 Flux (μ Jy)	Channel 3 Flux (μ Jy)	Channel 4 Flux (μ Jy)	α
215.9517579	24.0973808	5.609 ± 0.05	5.880 ± 0.06	5.963 ± 0.30	6.611 ± 0.31	-0.200 ± 0.003
215.9397962	24.0575490	13.764 ± 0.05	15.769 ± 0.06	19.672 ± 0.30	19.487 ± 0.31	-0.566 ± 0.043
215.9354755	24.0779616	7.590 ± 0.05	7.427 ± 0.06	7.531 ± 0.30	8.625 ± 0.31	-0.017 ± 0.050
215.9458471	24.0911789	15.937 ± 0.05	17.022 ± 0.06	15.636 ± 0.30	17.905 ± 0.31	-0.192 ± 0.051
215.9268477	24.0975650	15.264 ± 0.05	15.830 ± 0.06	15.460 ± 0.30	12.725 ± 0.31	0.012 ± 0.116
215.9688161	24.0841066	29.734 ± 0.05	54.470 ± 0.06	84.057 ± 0.30	183.671 ± 0.31	-2.498 ± 0.231
215.9342189	24.0683176	1.626 ± 0.05	2.238 ± 0.06	2.127 ± 0.30	4.656 ± 0.31	-1.281 ± 0.311
215.9683787	24.0852578	5.594 ± 0.05	6.819 ± 0.06	10.164 ± 0.30	7.092 ± 0.31	-0.711 ± 0.425
215.9504042	24.0820153	14.820 ± 0.05	15.812 ± 0.06	10.566 ± 0.30	13.276 ± 0.31	0.019 ± 0.437
215.9729404	24.0957611	1.448 ± 0.05	2.457 ± 0.06	2.809 ± 0.30	7.077 ± 0.31	-2.107 ± 0.438
215.9262837	24.0927605	8.800 ± 0.05	8.833 ± 0.06	9.290 ± 0.30	18.253 ± 0.31	-0.392 ± 0.629
215.9775090	24.0739197	1.611 ± 0.05	1.586 ± 0.06	1.110 ± 0.30	2.476 ± 0.30	-0.074 ± 0.671
215.9617739	24.1048934	15.508 ± 0.05	17.456 ± 0.06	12.332 ± 0.30	12.817 ± 0.30	-0.085 ± 0.676
215.9591515	24.1098108	9.437 ± 0.05	12.721 ± 0.06	26.109 ± 0.30	17.275 ± 0.31	-1.232 ± 0.717
215.9460311	24.0816273	20.359 ± 0.05	24.766 ± 0.06	18.337 ± 0.30	22.185 ± 0.30	-0.425 ± 0.735
215.9321221	24.0899281	24.573 ± 0.05	25.250 ± 0.06	13.636 ± 0.30	26.745 ± 0.31	0.073 ± 0.787
215.9732383	24.0983724	26.372 ± 0.05	29.005 ± 0.06	39.993 ± 0.30	16.673 ± 0.30	-0.090 ± 1.070
MS0451						
73.5525335	-3.0151069	21.817 ± 0.02	22.596 ± 0.03	22.395 ± 0.12	31.604 ± 0.13	-0.288 ± 0.458
73.5266952	-3.0365244	1.198 ± 0.02	1.983 ± 0.03	2.600 ± 0.12	5.976 ± 0.13	-2.053 ± 0.923
MS1054						
164.2609994	-3.6619864	125.759 ± 0.02	163.272 ± 0.04	191.572 ± 0.15	327.143 ± 0.17	-1.148 ± 0.145
164.2343897	-3.6099613	11.703 ± 0.02	14.129 ± 0.04	22.537 ± 0.15	25.869 ± 0.17	-1.001 ± 0.368
164.2447098	-3.6473231	39.975 ± 0.02	57.745 ± 0.04	66.941 ± 0.15	120.088 ± 0.17	-1.468 ± 0.535
164.2591409	-3.5959543	2.566 ± 0.02	2.951 ± 0.04	2.441 ± 0.15	3.777 ± 0.17	-0.457 ± 0.753
164.2702649	-3.6505658	1.533 ± 0.02	2.035 ± 0.04	3.923 ± 0.15	6.180 ± 0.17	-1.590 ± 0.839
164.2772592	-3.6190767	1.692 ± 0.02	2.392 ± 0.04	5.149 ± 0.15	8.099 ± 0.17	-1.862 ± 0.891
164.2814489	-3.6381497	11.625 ± 0.02	15.880 ± 0.04	16.480 ± 0.15	22.703 ± 0.17	-1.083 ± 1.063
SDSS1004						
151.1470122	41.1922362	3.002 ± 0.01	3.511 ± 0.02	3.766 ± 0.07	4.691 ± 0.07	-0.612 ± 0.524
151.1383888	41.2154740	29.172 ± 0.01	33.091 ± 0.02	35.597 ± 0.07	38.805 ± 0.07	-0.456 ± 0.620
151.1599021	41.2261194	8.808 ± 0.01	9.754 ± 0.02	10.441 ± 0.07	15.124 ± 0.07	-0.545 ± 0.896

Table 10: Multi-wavelength Comparison of AGN Detection Techniques

Cluster	#Variables	#IR Power Law	#IR Power Law	#X-ray PS	#X-ray PS	Var/IR	X-ray/IR	Var/X-ray
	Total	Total	w/opt. counterparts	Total	w/opt. counterparts			
<i>CL0152</i>	12	9	6	4	3	1 ^a	2 ^a	2 ^a
<i>CLJ1226</i>	20	8	6	6	6	0	1	0
<i>MACSJ0257</i>	13	-	-	1	1	-	-	0
<i>MACSJ0717</i>	19	18	13	9	7	1 ^a	1 ^a	3 ^a
<i>MACSJ0744</i>	18	-	-	12	6	-	-	2
<i>MACSJ0911</i>	14	-	-	5	4	-	-	1
<i>MACSJ1149</i>	13	-	-	2	2	-	-	1
<i>MACSJ1423</i>	24	17	15	10	9	0	0	2
<i>MACSJ2214</i>	8	-	-	1	3	-	-	0
<i>MS0451</i>	16	2	1	7	-	0	-	-
<i>MS1054</i>	11	7	4	8	3	0	3	0
<i>SDSS1004</i>	11	3	3	6	6	0	0	1

^a One object detected by all 3 techniques.

Table 11. Galaxies in the Lacy Wedge

Cluster	Galaxies	IR Power Law	Optical Variables	X-ray Point Sources
<i>CL0152</i>	65/267	9/9	2/5	4/4
<i>CLJ1226</i>	90/332	8/8	3/16	2/6
<i>MACSJ0717</i>	49/288	15/18	2/8	2/5
<i>MACSJ1423</i>	55/247	13/17	2/12	1/8
<i>MS0451</i>	42/293	2/2	0/8	2/6
<i>MS1054</i>	54/319	7/7	0/6	4/6
<i>SDSS1004</i>	56/251	3/3	1/9	3/6

Table 12: Cluster Spectroscopic Coverage

Cluster	# Redshifts	# Members	# Field	Redshift	Cluster Redshift Range [*]
<i>CL0152</i> ^a	81	48	33	0.831	0.82 - 0.87
<i>CLJ1226</i> ^b	42	25	17	0.888	0.90 - 0.91
<i>MACSJ0257</i> ^c	16	13	3	0.506	0.50 - 0.51
<i>MACSJ0717</i> ^c	125	108	17	0.548	0.53 - 0.56
<i>MACSJ0744</i> ^c	34	31	3	0.686	0.68 - 0.71
<i>MACSJ0911</i> ^c	24	21	3	0.504	0.49 - 0.52
<i>MACSJ1149</i> ^c	44	42	2	0.544	0.52 - 0.56
<i>MACSJ1423</i> ^c	45	36	9	0.545	0.53 - 0.56
<i>MACSJ2214</i> ^c	55	52	3	0.504	0.49 - 0.52
<i>MS0451</i> ^d	127	68	59	0.550	0.52 - 0.56
<i>MS1054</i> ^e	206	108	98	0.830	0.80 - 0.86
<i>SDSS1004</i>	3	3	-	0.680	-

^{*} Lowest-highest redshifts of confirmed cluster members from the literature

^a Demarco et al. (2005)

^b Ellis et al. (2006)

^c Barrett (2006)

^d Moran et al. (2007)

^e Tran et al. (2007), private communication

Table 13. AGN Redshifts ^a

Cluster	Var Cluster	Var Field	IR Cluster	IR Field	X-ray Cluster	X-ray Field
<i>CL0152</i>	1	1	2	0	2	1
<i>CLJ1226</i>	1	0	0	0	1	0
<i>MACSJ0257</i>	0	0	-	-	1	0
<i>MACSJ0717</i>	1	1	0	0	2	2
<i>MACSJ0744</i>	1	0	-	-	1	0
<i>MACSJ0911</i>	0	1	-	-	0	0
<i>MACSJ1149</i>	1	0	-	-	0	0
<i>MACSJ1423</i>	5	2	0	0	2	2
<i>MACSJ2214</i>	0	0	-	-	1	0
<i>MS0451</i>	3	2	1	0	-	-
<i>MS1054</i>	2	2	1	1	1	0
<i>SDSS1004</i>	-	-	-	-	-	-

^a A dash (-) indicates that data is not available.

Table 14. Percentage of Cluster AGN ^a

Cluster	% AGN _{weighted}	% AGN _{non-weighted}	% AGN _{spec}
<i>CL0152</i>	2.49 (21/889)	2.36 (21/889)	4.17 (2/48)
<i>CLJ1226</i>	3.13 (33/961)	3.43 (33/961)	8.0 (2/25)
<i>MACSJ0257</i>	1.0 (14/1535)	0.91 (14/1535)	7.7 (1/13)
<i>MACSJ0717</i>	2.27 (42/1813)	2.32 (42/1813)	2.78 (3/108)
<i>MACSJ0744</i>	2.13 (28/1430)	1.96 (28/1430)	3.23 (1/31)
<i>MACSJ0911</i>	1.35 (18/1353)	1.33 (18/1353)	x
<i>MACSJ1149</i>	0.92 (13/1512)	0.86 (13/1512)	2.38 (1/42)
<i>MACSJ1423</i>	3.75 (49/1337)	3.66 (49/1337)	20.0 (7/35)
<i>MACSJ2214</i>	0.81 (12/1373)	0.87 (12/1373)	1.92 (1/52)
<i>MS0451</i>	2.65 (25/1102)	2.27 (25/1102)	5.88 (4/68)
<i>MS1054</i>	2.29 (23/893)	2.58 (23/893)	2.78 (3/108)
<i>SDSS1004</i>	1.43 (20/1651)	1.21 (20/1651)	-
Mean	2.01 \pm 1.4	1.98 \pm 1.4	5.88 \pm 2.3
Median	2.27 \pm 1.5	2.27 \pm 1.5	4.17 \pm 2.0

^a A dash (-) indicates that data is not available; an x indicates there are no AGN detected, though data exist.

Table 15: Percentage of Cluster AGN By Type

Cluster	% AGN _{weighted}	% AGN _{spec}
Variables		
<i>CL0152</i>	1.37 (12/889)	2.08 (1/48)
<i>CLJ1226</i>	2.05 (20/961)	4.0 (1/25)
<i>MACSJ0257</i>	0.92 (13/1535)	-
<i>MACSJ0717</i>	1.04 (19/1813)	0.93 (1/108)
<i>MACSJ0744</i>	1.38 (18/1430)	3.23 (1/31)
<i>MACSJ0911</i>	1.05 (14/1353)	x
<i>MACSJ1149</i>	0.86 (12/1512)	2.38 (1/42)
<i>MACSJ1423</i>	1.89 (24/1337)	14.29 (5/35)
<i>MACSJ2214</i>	0.61 (8/1373)	x
<i>MS0451</i>	1.65 (16/1102)	4.41 (3/68)
<i>MS1054</i>	1.08 (11/893)	1.85 (2/108)
<i>SDSS1004</i>	0.80 (11/1651)	-
IR Power Law		
<i>CL0152</i>	1.16 (9/889)	4.17 (2/48)
<i>CLJ1226</i>	0.53 (8/961)	x
<i>MACSJ0257</i>	-	-
<i>MACSJ0717</i>	0.98 (18/1813)	x
<i>MACSJ0744</i>	-	-
<i>MACSJ0911</i>	-	-
<i>MACSJ1149</i>	-	-
<i>MACSJ1423</i>	1.36 (14/1337)	x
<i>MACSJ2214</i>	-	-
<i>MS0451</i>	0.23 (2/1102)	1.47 (1/68)
<i>MS1054</i>	0.62 (7/893)	0.93 (1/108)
<i>SDSS1004</i>	0.21 (3/1651)	-
X-ray		
<i>CL0152</i>	0.49 (4/889)	4.17 (2/48)
<i>CLJ1226</i>	0.65 (6/961)	4.0 (1/25)

Table 15. Continued

Cluster	% AGN _{weighted}	% AGN _{spec}
<i>MACSJ0257</i>	0.08 (1/1535)	7.69 (1/13)
<i>MACSJ0717</i>	0.43 (9/1813)	1.85 (2/108)
<i>MACSJ0744</i>	0.93 (12/1430)	3.23 (1/31)
<i>MACSJ0911</i>	0.38 (5/1353)	x
<i>MACSJ1149</i>	0.12 (2/1512)	x
<i>MACSJ1423</i>	0.67 (10/1337)	5.71 (2/35)
<i>MACSJ2214</i>	0.20 (4/1373)	1.92 (1/52)
<i>MS0451</i>	0.77 (7/1102)	x
<i>MS1054</i>	1.0 (8/893)	0.93 (1/108)
<i>SDSS1004</i>	0.42 (6/1651)	-